Photoplethysmogram and Phonocardiogram Integrated Circuits for Multi-mode Healthcare System on the Chest with Vascular Transit Time based Blood Pressure Estimation

Minseok Park

Department of Electrical Engineering

Ulsan National Institute of Science and Technology

Photoplethysmogram and Phonocardiogram Integrated Circuits for Multi-mode Healthcare System on the Chest with Vascular Transit Time based Blood Pressure Estimation

A thesis/dissertation submitted to

Ulsan National Institute of Science and Technology

in partial fulfillment of the

requirements for the degree of

Master of Science

Minseok Park

11.30.2022 of submission
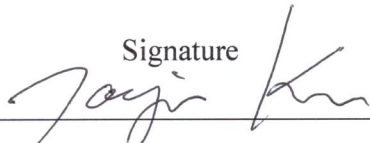
Approved by

Advisor

Jae Joon Kim

Photoplethysmogram and Phonocardiogram Integrated Circuits for Multi-mode Healthcare System on the Chest with Vascular Transit Time based Blood Pressure Estimation

Minseok Park

This certifies that the thesis/dissertation of Minseok Park is approved.

11.30.2022 of submission

Signature

Advisor: Jae Joon Kim

Signature

Thesis Committee member #1 : Yunsik Lee

Signature

Thesis Committee member #2 : Hoon Eui Jeong

Signature

Abstract

Blood Pressure is the most important physiological signal because it is highly associated with various cardiovascular diseases, and it is the basic index to monitor these kinds of diseases. Among various blood pressure measurement methods, Vascular Transit Time (VTT)-based blood pressure estimation method utilizes Photoplethysmogram (PPG), which is the physiological signal from blood volume changes using light, and Phonocardiogram (PCG), which is the cardiac signal corresponding to heart beat sound. In order to continuous blood pressure monitoring in our daily life, real-time VTT monitoring system with PPG and PCG integrated circuit would be excellent solution. The requirements of this system include low-power consumption for long-term operation with a small-sized battery, low-noise characteristic for accurate signal acquisition, and unobstructed measurement position in order to avoid cumbersome. Also, VTT is defined as the time interval between the PCG peak and the PPG peak, peaks of the two signals are needed in VTT calculation.

This master's thesis proposes a readout integrated circuit (ROIC) which achieves low-power consumption, low-noise performance, and easy signal processing. PPG ROIC consists of an LED driver that can control the intensity of the LED and a Light-to-Digital Converter (LDC) operating with a dual-slope mechanism, which converts the photodiode current from a reflected light to digital data. Since the LDC directly converts light into digital, it does not require an additional ADC and suitable for low-power applications. During dual-slope operation, the noise performance is limited by the main integrator and comparator. For low-noise operation, the noise of the core amplifier of the main integrator is reduced by the chopper-stabilization technique, and the quantization noise of the comparator is shaped through a noise-shaping loop. In the noise-shaping loop, the practical noise-shaping performance is reduced due to the charge sharing problem that occurs during the operation of residue voltage save. To solve this problem, an improved noise-shaping loop is proposed.

To calculate the VTT, the PCG peak and PPG peak are determined through the digital signal processing in the microcontroller unit (MCU). However, the process of determining the peak only through the shape of the signal waveform alone requires significant processing burden and high-power consumption in the MCU. Especially, for PCG signals, it is very challenging to distinguish different peaks of similar amplitude. Thus, the PCG S1 peak and PCG S2 peak are distinguished respectively using the proposed dual peak detector consisting of a parallel envelope detector and a sort algorithm block.

The system for monitoring blood pressure on the chest is implemented with the proposed PPG and PCG integrated circuits. The prototype operates using a battery, and can measure a small chest PPG signal and obtain a PCG signal without using a stethoscope. Through this, it achieves a miniaturized

Contents

List of Figures

Nomenclature

ROIC   Readout integrated circuit

AFE   Analog front-end

VTT   Vascular transit time

ET   Ejection rime

SBP   Systolic blood pressure

DBP   Diastolic blood pressure

PPG   Photoplethysmogram

PCG   Phonocardiogram

CCIA   Capacitive-coupled instrumentation amplifier

PGA   Programmable-gain amplifier

LDC   Light-to-digital converter

DAC   Digital-to-analog converter

SAR   Successive approximation register

ADC   Analog-to-digital converter

SPI   Serial peripheral interface

MCU   Microcontroller unit

DSP   Digital signal processing

LPF   Low-pass filter

SNR   Signal-to-noise ratio

DR   Dynamic range

IoT   Internet of tings

Chapter I

Introduction

1.1 Motivation

Figure 1.1. Interest in digital healthcare under development of technology and the aging society

Nowadays, the demand for healthcare preventing and monitoring various diseases is steadily increased, so interest in the healthcare industry is growing. Meanwhile, the low fertility rate and increase in life expectancy cause rapid aging society and emerge as major social issues. Accordingly, efforts to solve these problems with the development of technology has continued, and a digital healthcare industry is appeared, which incorporate digital technology into the healthcare industry [1]. In particular, post COVID-19 pandemic drives digital innovation, and accelerates the development of various types of wearable devices.

Among various vital signs, blood pressure is associated with many diseases such as dizziness, syncope or hypertension, and these diseases can be prevented by the continuous blood pressure monitoring [2]. However, a conventional blood pressure measurement method is to apply air pressure using a blood pressure gauge, which is not suitable for continuous blood pressure monitoring [3]. Therefore, several blood pressure estimation methods have been proposed, and one suitable method is to use vascular transit time. Photoplethysmogram and phonocardiogram signals are needed to

obtain the vascular transit time. Using photoplethysmogram and phonocardiogram integrated circuits, vascular transit time-based blood pressure estimation method can be applied to wearable devices. Since wearable devices usually operate using batteries, it is necessary to implement a low-power, low-noise system. In addition, an appropriate measurement position for signal acquisition should be selected so that the device does not interfere with daily life.

Figure 1.2. Various wearable devices applicable to blood pressure measurement

In this paper, a miniaturized multi-mode wearable healthcare system on the chest with vascular transit time-based blood pressure estimation, is proposed.

To this end, a low-power low-noise light-to digital converter for photoplethymogram on the chest and dual peak detector which make a signal processing easily for phonocardiogram, are introduced.

1.2 Thesis organization

This thesis proposes a photoplethysmogram and phonocardiogram integrated circuits for healthcare system on the chest with vascular transit time-based blood pressure estimation, and it is organized into five chapters.

Chapter I spotlights the research motivation.

Chapter II introduces the conceptual background of photoplethysmogram and phonocardiogram signals, and the relationship between blood pressure and vascular transit time. And the requirements are described for photoplethysmogram and phonocardiogram readout circuits to implement the proposed vascular transit time-based blood pressure monitoring system on the chest.

Chapter III proposes a high performance light-to digital converter for photoplethysmogram on the chest and a dual peak detector for different peaks of phonocardiogram. The operation of the proposed dual-slope light-to digital converter and the applied low-noise circuit techniques are introduced. A dual peak detector to distinguish S1 and S2 peaks of phonocardiogram, is also introduced.

Chapter IV describes the experimental results of the proposed photoplethysmogram and phonocardiogram integrated circuits. A system implementation that supports three modes with the prototype is shown. A comparison with a commercial blood pressure gauge also conducted to verify the accuracy of estimated blood pressure.

Finally, Chapter V discusses the conclusions on the results and summarizes the thesis.

Chapter II

Background

2.1 Photoplethysmogram

2.1.1 Photoplethysmogram signal characteristic
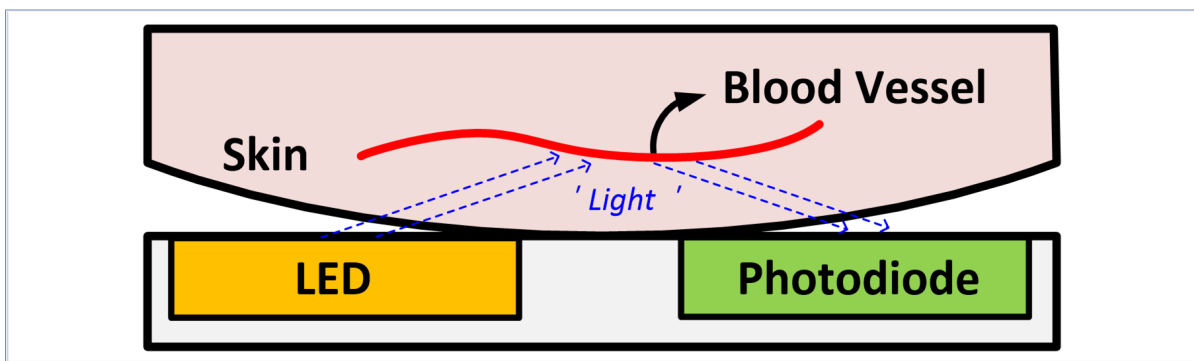
Figure 2.1. Measurement method of the PPG signal

Photoplethysmogram (PPG) is widely used as non-invasive measurement method on the surface of the skin. PPG is an optically measured plethysmogram which can show information about blood volume changes of the pulsatile arterial blood [4]. In order to measure the PPG signal, two components are needed: a light emitting source and an optical receiver. Typically, an LED is used for the light source and a photodiode for the optical receiver. Various types of light can be used in LED, and characteristics are different depending on the wavelength of the light. The light with long wavelength has high penetration rate then suitable for thick tissue, and the short one is only affected by surface tissue movement, not deep tissue, then it has high motion artifact immunity [5]. Figure 2.1 shows the measurement method of the PPG signal. The light emitted from the LED is absorbed or reflected from tissue and blood vessel, then the signal can be measured through the photodiode current from a reflected light. The light reflection rate is inversely related to its absorption rate. When a large amount of blood flows in the blood vessels, the absorbed light increases and the reflected light into the photodiode decreases. In contrast, when a small amount of blood flows, the absorbed light decreases and the reflected light increases.
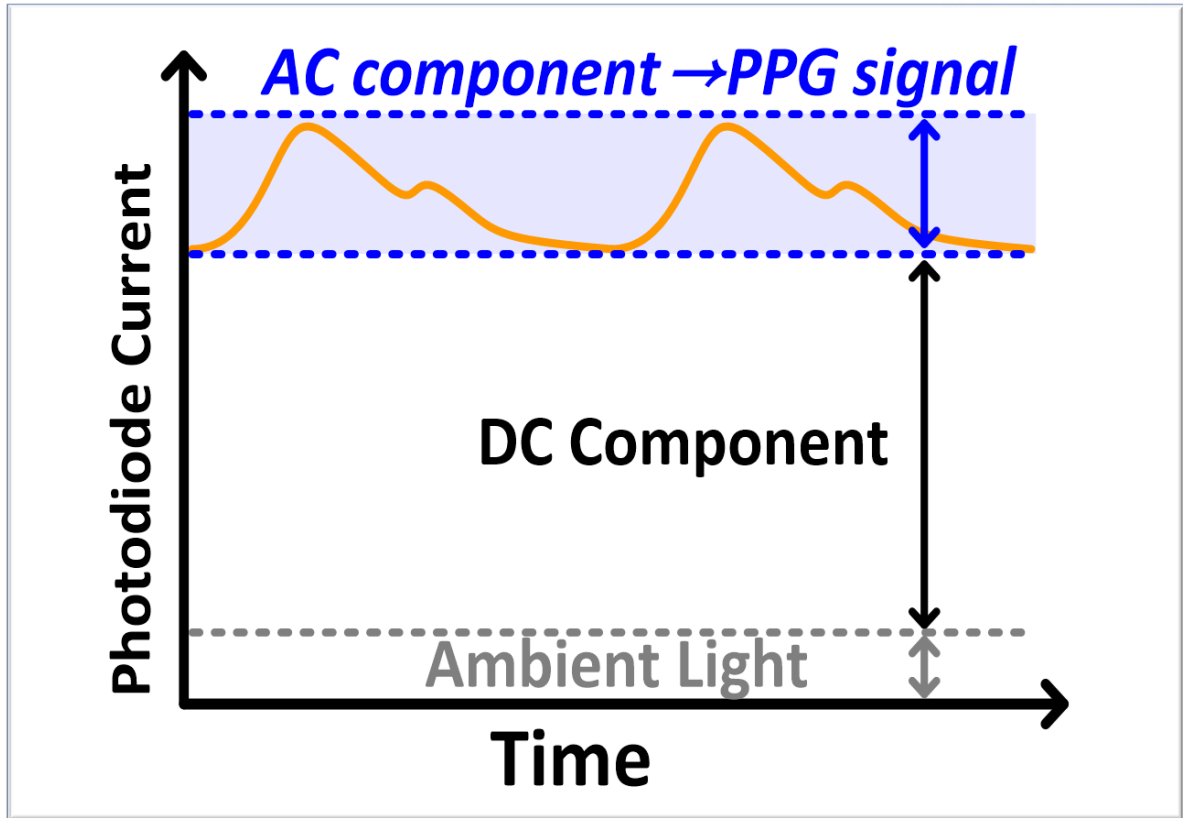
Figure 2.2. Various components of the photodiode current waveform

The current generated by the photodiode consists of various components [6], as shown in figure 2.2. Ambient light is unwanted light from the external measurement environment. The DC component is determined by tissue thickness, average blood volume, and skin color, etc. This value does not change in a fixed measurement environment due to a constant amount of light absorption. The AC component is a pulsatile physiological waveform, which is the amount of the change of absorbed light by the change in blood volume. This AC component is called the PPG signal, and the typical frequency range is 0.5Hz to 5Hz [7]. The photodiode current consists of a small AC component superimposed on the large DC component. Therefore, PPG ROIC should have a wide dynamic range with large DC baseline cancellation, and ambient light should also be cancelled for accurate signal readout.

2.1.2 Difficulties of photoplethysmogram readout on the chest
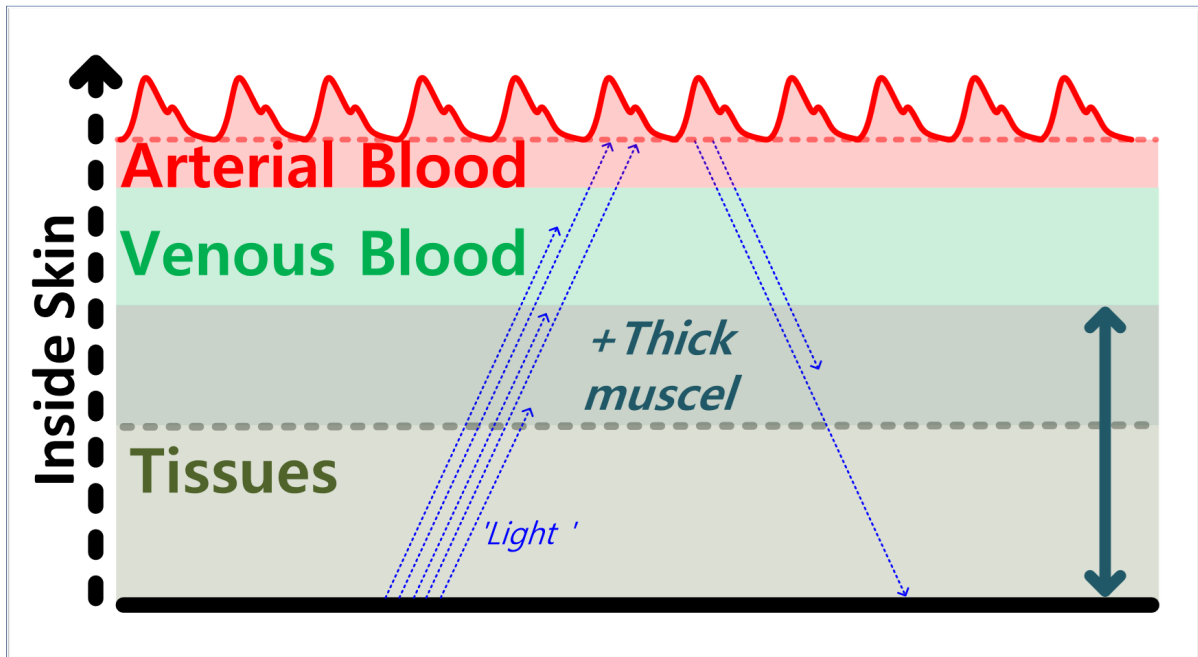
Figure 2.3. Internal anatomy of skin and light attenuation due to thick muscle

The amount of the absorbed light is different depending on the thickness of the tissue, then the photodiode current from a reflected light is also different [8]. As the thickness of the tissue increases, the amount of the absorbed light increases, and the total amount of reflected light decreases because of the attenuated light. On the other hand, the DC component of the photodiode current increases since the ratio of the reflected light from the thick tissue increases. That is, in thick tissue, the total photodiode current decreases, and the ratio of the DC component increases. For example, the chest has thick tissue since it is covered with thick muscle tissue. Accordingly, the distance between the sensor and the blood vessel increases, and the light emitted from the LED is highly attenuated by the thick tissue. As a results, the PPG signal has a small signal amplitude. On the contrary, the fingertip is covered with thin tissue, then the distance between the sensor and the blood vessel decreases. So, the finger PPG signal has a high signal amplitude and is widely used as a reference for the measurement position.

In our wearable device application, the chest PPG should be adopted for convenient usability and integrated device. Therefore, the PPG ROIC of the system must have a high SNR to measure chest PPG.

2.2 Phonocardiogram

2.2.1 Phonocardiogram signal characteristic
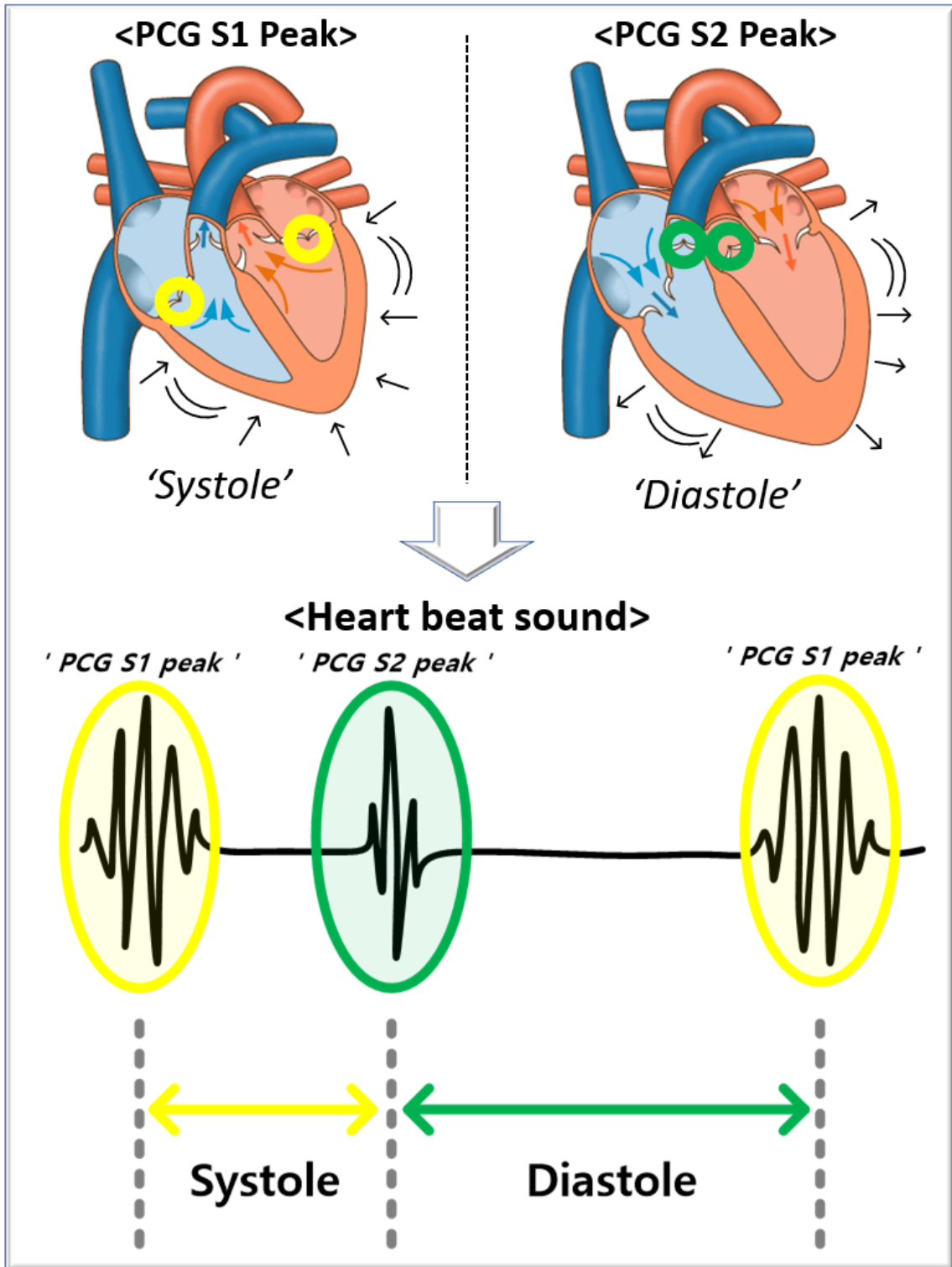
Figure 2.4. Principle of the PCG S1 peak and PCG S2 peak with the movement of the human heart

7

Phonocardiogram (PCG) is the sound signal of heart-beat generated by the circulatory movement of the heart that pumps out blood to the rest of body and lungs. If this heart-beat sound is measured through a microphone, the signal can be recorded and processed as an electrical waveform. The heart-beat sound is a vibration sound that are produced by the collision of the heart valves with each other, when they are closed to prevent the flow of blood. This collision sound occurs twice in one heart-beat period, so the PCG waveform has two different peaks in one period.

The first peak is generated at the beginning of systole. In systole, blood is transferred from the heart to the arteries. In this process, oxygen can be supplied to the rest of body by oxygen-rich blood flowing through the aorta, and oxygen can be obtained from the lungs by oxygen-poor blood flowing through the pulmonary artery. At this time, in order to prevent the backflow of blood from the ventricle to the atrium, the tricuspid valve and the mitral valve, which are atrioventricular valve, are closed and the collision sound occurs. This sound can be checked as a peak in the PCG waveform. This peak is called the S1 peak of the PCG signal.

Oxygen-poor blood from the rest of body flows into the atrium through veins, and oxygen-rich blood from lungs flows into the atrium through the pulmonary veins.

The second peak is generated at the beginning of diastole and the end of systole. In diastole, blood is transferred from each atrium to the ventricle. At this time, in order to prevent the flow of blood from the ventricle to the artery, the aortic valve and the pulmonary valve, which are semilunar valve, are closed and the collision sound occurs again. This sound can be checked as another peak in the PCG waveform. This peak is called the S2 peak of the PCG signal.

Figure 2.4 shows the principle of S1 and S2 peaks of PCG with the movement of the human heart, as previously mentioned. The PCG S1 peak has a frequency range of 50Hz to 150Hz, and the PCG S2 peak has a frequency range of 50Hz to 200Hz [9]. The time interval between the PCG S1 peak and the PCG S2 peak (systole) is shorter than the time interval between the PCG S2 peak and the next PCG S1 peak (diastole). Through this time difference or comparing the peak positions with the peaks of other signals such as ECG or PPG, it can be possible to distinguish the PCG S1 peak and the PCG S2 peak.

2.3 Vascular transit time-based blood pressure estimation

2.3.1 Non-invasive blood pressure estimation overview
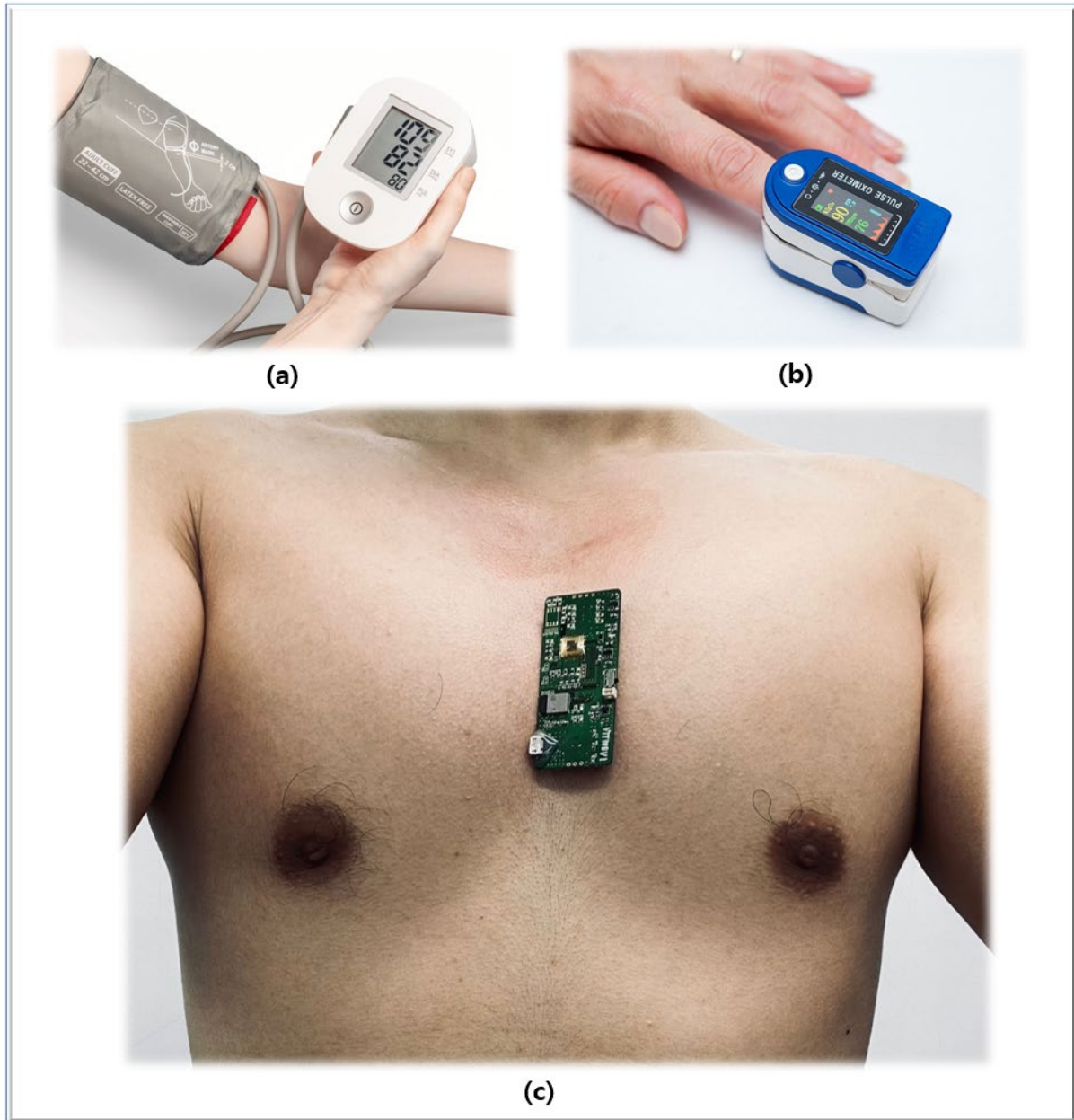
Figure 2.5. Various non-invasive blood pressure estimation methods through (a) Oscillometry, (b) Pulse Wave Analysis, and (c) Vascular Transit Time

Early blood pressure measurement methods were invasive. This method directly measures blood pressure of the artery by inserting a cannula needle into the artery [10]. It can make a continuous blood pressure monitoring possible, but it requires surgery and the surgical site could be infected, so currently

9

not used well. Therefore, non-invasive blood pressure measurement method is widely used, nowadays. There are three non-invasive blood pressure measurement methods, as shown in figure 2.5. First one is the oscillometric method. The principle of this method is that a cuff is put on the arm and external air pressure is applied to the artery [11]. Through the deflation of the inflated cuff, the blood pressure can be measured with the pressure sensor. This method has a very good accuracy, but it must need a cuff and a continuous blood pressure monitoring is impossible. For earlier detection of cardiovascular problem in patients with blood pressure disorders, a continuous blood pressure monitoring system is necessary. Also, the device should be conveniently wearable and not interfere with daily life. But this method cannot be applied to wearable devices. Second one is the pulse wave analysis method. This method utilizes the PPG waveform. The PPG waveform is correlated with the blood pressure waveform. Through the algorithm-based pre-calibration using the PPG waveform and pre-measured blood pressure data, the blood pressure can be estimated from the PPG waveform [12]. This method could be applied to wearable devices since cuff-less, continuous blood pressure monitoring is possible. However, the blood pressure is estimated only through the shape of the PPG waveform alone, so it has poor accuracy. Third one is the vascular transit time-based method. This method utilizes the time difference between the PCG peak and the PPG peak. Since this time difference is highly correlated with the blood pressure, it can be calculated by substituting the time difference to a pre-calibrated equation [13]. This method has good accuracy, and cuff-less, continuous blood pressure monitoring is possible. Therefore, it can be a great solution applied to an accurate wearable blood pressure monitoring system.

2.3.2 Relationship of blood pressure with vascular transit time

As I mentioned above, the blood pressure is highly correlated with the time difference between the PCG peak and the PPG peak. The time difference between the PCG S1 peak and the PPG peak is the Vascular Transit Time (VTT), and the time difference between the PCG S1 peak and the PCG S2 peak is the Ejection Time (ET). As shown in figure 2.6, when the blood pressure is low, such as taking a rest, VTT is shorter, and when the blood pressure is high, such as taking an exercise, VTT is longer. Blood pressure is inversely related to VTT, and utilizing this relationship, the blood pressure can be calculated from the PCG peaks and the PPG peak. The equation is shown in (2.1) [13],

$$SBP = SBP_0 - VTT \times 425$$
$$DBP = SBP - \frac{K_1 + 0.25 \times (ET - 35)}{K_2} \qquad (2.1)$$

where SBP is the systolic blood pressure that is the pressure exerted on the arteries when the heart

contracts, and DBP is the diastolic blood pressure that is the pressure exerted on the arteries when the heart relaxes. Both of the blood pressure are expressed in mmHg. VTT and ET are expressed in millisecond. $[\ ]_0$ is the constant obtained from experimentally. K_1, K_2 are individual parameters determined by height, weight, and age of the subject.
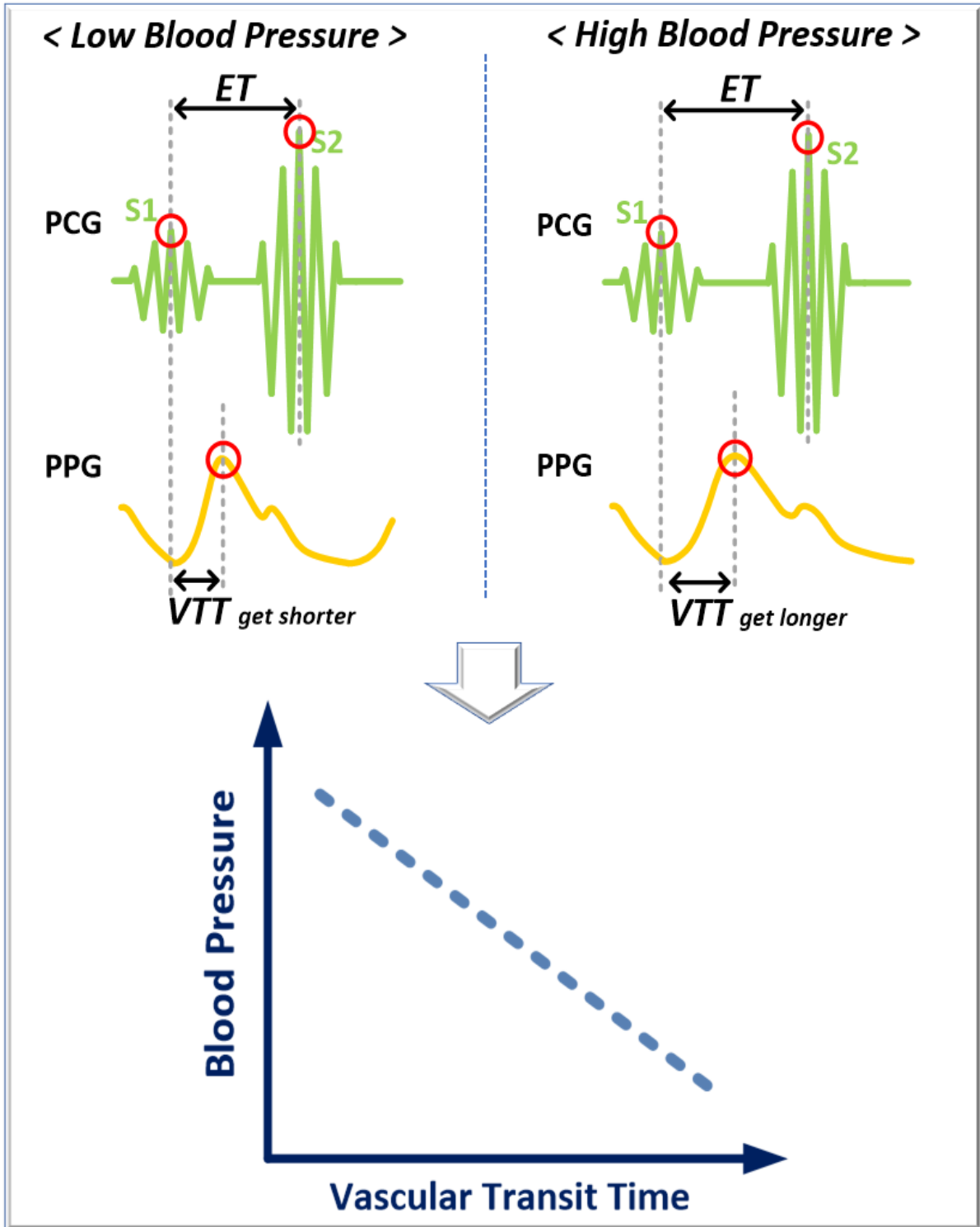
Figure 2.6. Relationship between vascular transit time and blood pressure

Chapter III

PPG and PCG integrated circuit for VTT monitoring system
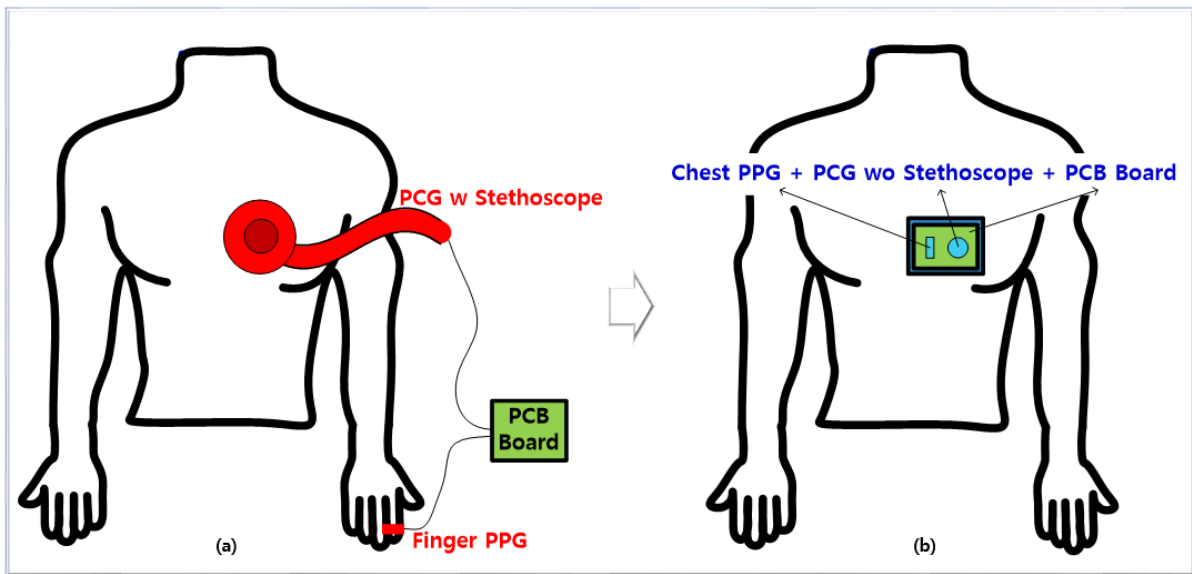
Figure 3.1. (a) Previous VTT-based blood pressure monitoring system and
(b) Proposed miniaturized chest VTT-based wearable blood pressure monitoring system

For continuous blood pressure monitoring in daily life, the measurement device should not interfere with our activities. To this end, the system should be implemented in wearable device and measure the signal conveniently. However, as shown in figure 3.1, the previous VTT-based blood pressure monitoring system utilizing PPG and PCG signals cannot achieve this requirement [14]. Since PCG signal measurement in the previous system should be needed a stethoscope, the long drooping tube of stethoscope and large diaphragm make it uncomfortable to measure signals on the chest with the sensor. In addition, finger PPG prevents one hand from being used, then normal activities are impossible. Therefore, the previous VTT-based blood pressure monitoring system could not be implemented in a wearable device and is not suitable for continuous blood pressure monitoring in daily life.

In this thesis, a chest VTT-based blood pressure monitoring system is proposed with a miniaturized wearable device, utilizing advanced low-power, low-noise circuit techniques. The proposed system measures the PPG signal on the chest instead of the finger, and measures the PCG signal without using a stethoscope. Consequently, PPG and PCG sensors can be integrated on a single PCB substrate and implemented as a miniaturized wearable device.
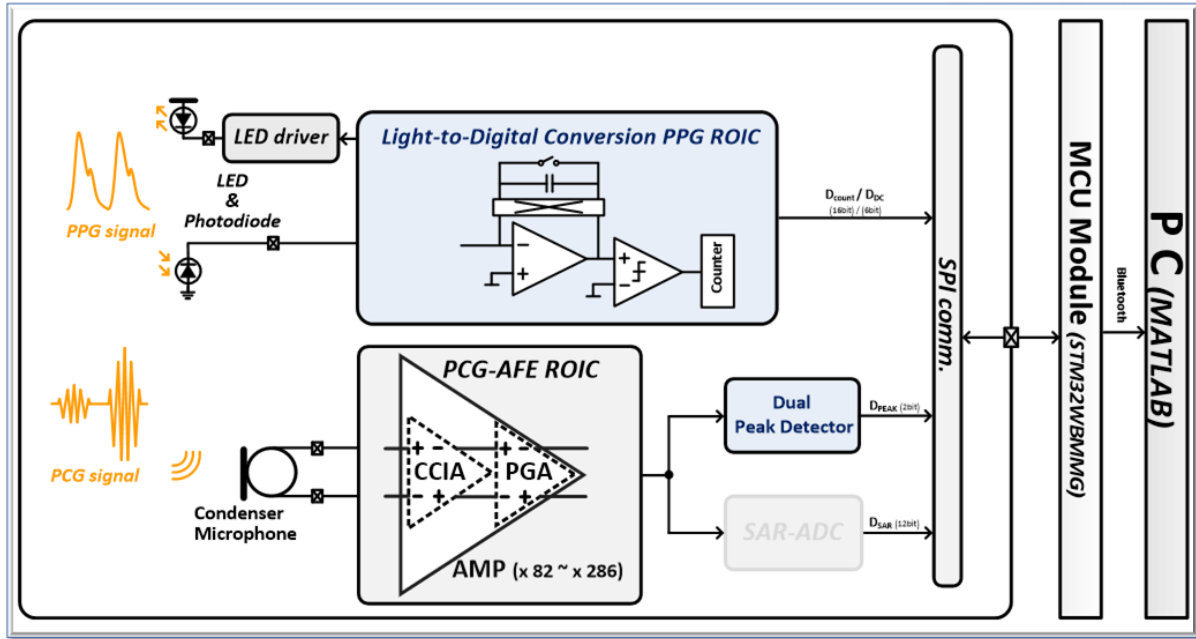
Figure 3.2. Proposed overall system block diagram for PPG and PCG monitoring

Figure 3.2 shows the proposed overall system block diagram for PPG and PCG monitoring. The proposed system consists of PPG and PCG readout integrated circuit (ROIC). PPG ROIC consists of a dual-slope light-to-digital converter (LDC) [15], that is a low-power readout circuit, since it does not require additional analog-to-digital converter (ADC). Also, low-noise circuit techniques are adopted for measuring the small chest PPG signal, and an LED driver to control LED is included. The correct PPG signal is acquired by mapping the DC bits (D_{DC}) with the COUNT bit (D_{COUNT}). But this mapping process is difficult to be implemented in ROIC, because the weight of the DC bits varies depending on the setting of the internal timing block. Also, the PPG signal is greatly affected by the motion artifact and the movement of the chest is large due to breathing. Therefore, the peak detection of the PPG signal is implemented by the digital signal processing (DSP) in the microcontroller unit (MCU).

PCG analog front-end (AFE) consists of a capacitive-coupled instrumentation amplifier (CCIA) and a programmable gain amplifier (PGA), and can be shared with ExG channel, since various low-noise circuit techniques are applied. To distinguish between the PCG S1 and PCG S2 peak, a new dual peak detector is proposed. And the PCG waveform can be checked through SAR-ADC as needed. The ROIC is controlled through the MCU using serial peripheral interface (SPI) communication, and the measurement results are shown in PC MATLAB program.

13

3.1 Proposed high performance PPG ROIC
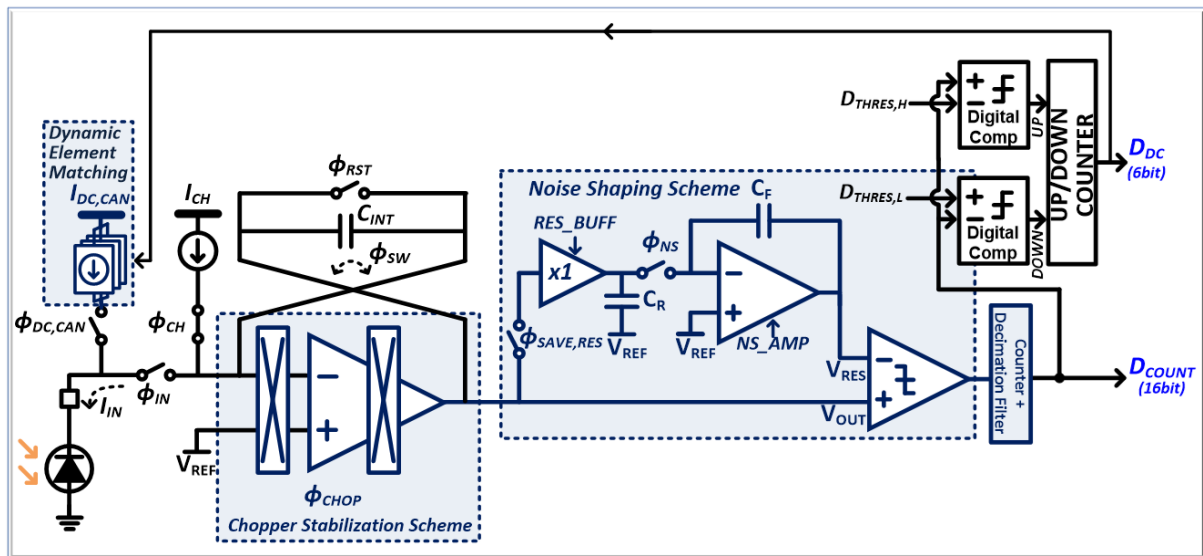
Figure 3.3. System architecture of the proposed chopper-stabilized improved noise-shaping LDC

For the chest PPG readout, high SNR is required for ROIC, and the system should be possible operated on battery-powered for application to wearable devices. Therefore, in this chapter, a low-power, low-noise PPG ROIC is proposed. Figure 3.3 shows the system architecture of the proposed chopper-stabilized improved noise-shaping LDC. This system is based on dual-slope mechanism, which is operated on a charging phase and a discharging phase. Through dual-slope operation, the photodiode current from a reflected light is directly converted to digital data, so it can have low-power consumption because additional ADC is not required. The large DC baseline of the PPG signal is adaptively cancelled with an auxiliary current path and up/down counter which feedbacks the result of the converted data. Also, the ambient light is cancelled by the switching operation of the capacitor of the main integrator. The proposed system can achieve high SNR by adopting low-noise circuit techniques such as chopper-stabilization and improved noise-shaping loop.

3.1.1 Operation of the proposed LDC
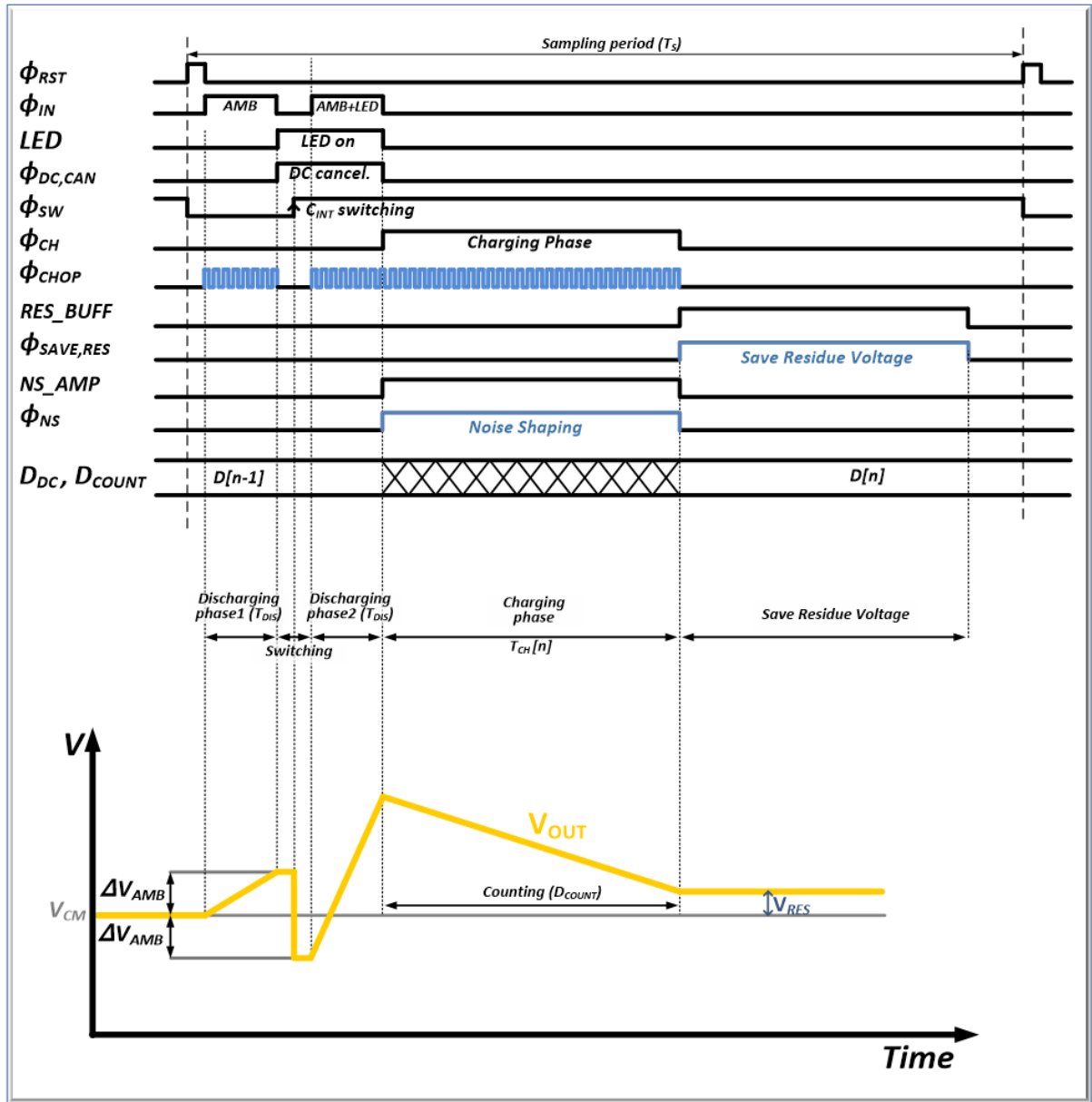
Figure 3.4. Timing diagram of the proposed LDC

Figure 3.4. shows the timing diagram of the proposed LDC. First, when sampling starts, reset signal (ϕ_{RST}) reset the circuits to its initial state. Second, a capacitor C_{INT} of the main integrator is discharged by the input current (ϕ_{IN}) which consists of the only ambient light from the photodiode with the LED off. Third, for ambient light cancellation, the connection of C_{INT} is reversed (ϕ_{SW}). Then, with the LED on (*LED*), C_{INT} is discharged again by the input current from photodiode which consists of the combination of ambient light and LED. Therefore, if the discharging time of two discharging phase is same, the effect of the ambient light can be easily eliminated, just the reversing operation of C_{INT}. For

15

the moment, when the LED is turned on, the amplitude of the DC input current is increased because the intensity of a reflected light is increased. So, the large baseline current should be removed using adaptively controlled $I_{DC,CAN}$ ($\phi_{DC,CAN}$).

Fourth, through the dual-slope operation which is the process of charging the discharged capacitor using I_{CH} (ϕ_{CH}), the photodiode current from a reflected light can be directly converted to digital data. At this time, the noise-shaping loop is operated to shape the quantization noise (ϕ_{NS}). In a charging phase and a discharging phase, the noise of the core amplifier of main integrator is reduced by applying chopper-stabilization technique (ϕ_{CHOP}). Finally, the residue voltage is saved in the residue voltage save capacitor C_R ($\phi_{SAVE,RES}$) after conversion is completed (D_{DC}, D_{COUNT}). On the other hand, the power consumption can be reduced by turning on the noise-shaping amplifier and residue voltage driving buffer only when the noise-shaping Loop operates (*NS_AMP*) and the residue voltage is saved (*RES_BUFF*), respectively. Also, since LED duty-cycle can be controlled from 0.25% to 1%, the power consumption of the LED driver is significantly reduced.

3.1.2 Noise analysis of previous dual-slope LDC
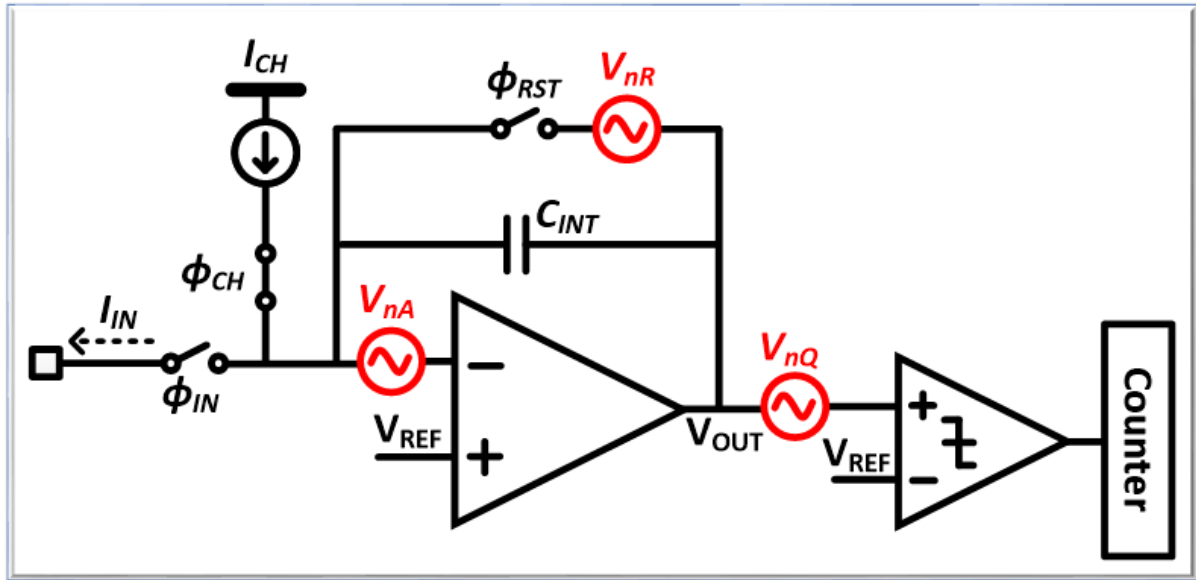
Figure 3.5. Noise modeling of a conventional dual-slope LDC

Although the dual-slope structure has a slow digital conversion speed, a high effective number of bits (ENOB) can be achieved with a simple circuit design. So, it is suitable for low-speed but accurate applications. In addition, if the integrator is shared and the comparator and counter are designed separately for each channel, it can be easy to implement multi-channel interface. Therefore, it is widely used in the sensor interface circuits. Meanwhile, there are three noise components that limit the noise performance of a conventional dual-slope LDC. Figure 3.5 shows the noise modeling of a conventional dual-slope LDC: a reset switch noise (V_{nR}), the noise of the core amplifier (V_{nA}) and the quantization noise (V_{nQ}).

First, a reset switch noise is the thermal noise from the reset switch of the main integrator, and shown in equation (3.1).

$$\overline{V_{nR}}^2 = \frac{kT}{C_{INT}} \tag{3.1}$$

This noise is generated by the reset switch which reset a capacitor C_{INT} of the integrator, before every sampling period. Fortunately, in a typical PPG readout system, this noise component is negligible, because C_{INT} is used in large enough (>100pF).

Second, the flicker noise and thermal noise of the core amplifier is shown in equation (3.2).

$$\overline{V_{nA}}^2 = \frac{4kT}{g_m}\left(1 + \frac{f_c}{f}\right) \qquad (3.2)$$

where f_C is the corner frequency of the flicker noise. On the other hand, the transfer function of a duty-cycled integration of the dual-slope integration on the capacitor C_{INT} during a period Δt is equation (3.3).

$$V_o(f) = \frac{I_{in}}{C_{INT}} \cdot \Delta t \cdot sinc(\pi f \Delta t) \qquad (3.3)$$

Then the output noise of the core amplifier of the integrator is expressed in equation (3.4).

$$\begin{aligned}
\overline{V_{nO}}^2 &= \frac{\overline{I_{nA}}^2}{C_{INT}^2} \cdot \int_0^\infty t_{INT}^2 \cdot sinc(\pi f t_{INT})^2 \, df \\
&= (g_m^2 \cdot \overline{V_{nA}}^2) \cdot \frac{1}{C_{INT}^2} \cdot \int_0^\infty t_{INT}^2 \cdot sinc(\pi f t_{INT})^2 \, df \\
&= 4kT g_m \left(1 + \frac{f_c}{f}\right) \cdot \frac{1}{C_{INT}^2} \cdot \int_0^\infty t_{INT}^2 \cdot sinc(\pi f t_{INT})^2 \, df \\
&\cong 4kT g_m \cdot \frac{t_{INT}^2}{C_{INT}^2} \cdot \frac{1}{\pi t_{INT}} \cdot \left\{\frac{\pi}{2} + \pi t_{INT} \cdot f_c \ln f_c\right\} \\
&\cong 2kT g_m \cdot \frac{t_{INT}}{C_{INT}^2} \qquad (3.4)
\end{aligned}$$

where t_{INT} is the total integration time. This output noise should be concerned.

Third, the quantization noise is generated by the operation of the comparator, and shown in equation (3.5).

$$\overline{V_{nQ}}^2 = \frac{LSB^2}{12} = \frac{1}{12} \cdot \left(\frac{I_{CH}}{C_{INT} \cdot f_{COMP}}\right)^2 \qquad (3.5)$$

where f_{COMP} is the operating frequency of the comparator. For low-power operation, the maximum clock speed is limited, then the quantization noise cannot be negligible.

Consequently, the total output noise of a conventional dual-slope LDC consists of two dominant components: the noise of the core amplifier, the quantization noise (3.6).

$$\overline{V_{nO}}^2 = 2kT g_m \cdot \frac{t_{INT}}{C_{INT}^2} + \frac{1}{12} \cdot \left(\frac{I_{CH}}{C_{INT} \cdot f_{COMP}}\right)^2 \qquad (3.6)$$
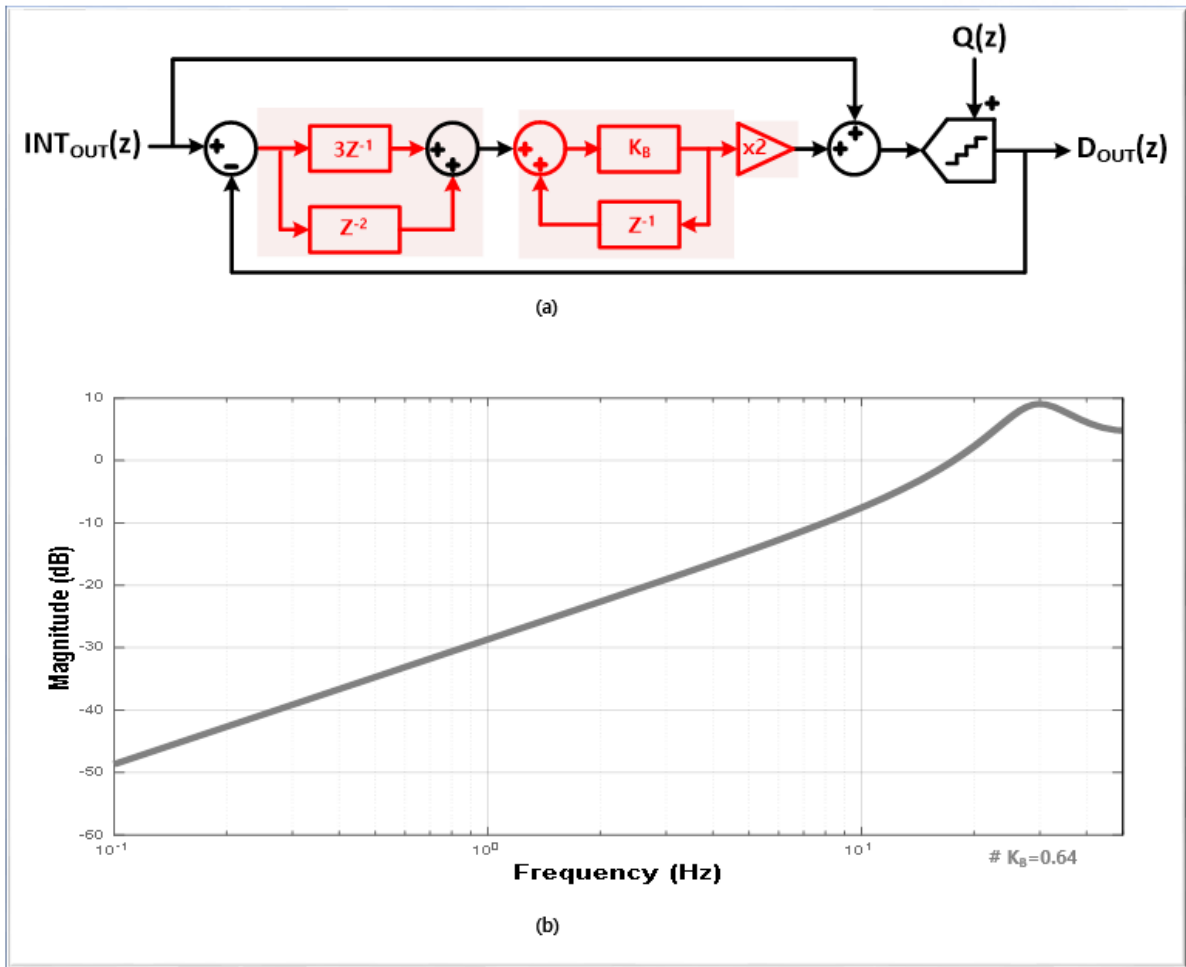
Figure 3.6. (a) The behavior model and (b) the plot of the noise transfer function of the previous noise-shaping dual-slope LDC

There are continuous researches to improve the performance of dual-slope LDC. Among two dominant noise components of the dual-slope LDC, [16] reduces the quantization noise by a 2nd-order noise-shaping loop, and the overall transfer function is shown in equation (3.7).

$$D_{OUT}(z) = INT_{OUT}(z) + \frac{(1 - z^{-1})}{1 + (2K_B - 1) \cdot z^{-1} + \frac{2}{3}K_B \cdot z^{-2}} Q(z) \tag{3.7}$$

The behavior model and the plot of the noise transfer function of the previous noise-shaping dual-slope LDC is shown in figure 3.6, and it shows good noise-shaping performance. However, this previous noise shaping dual-slope LDC has four problems.

First, too large capacitor is needed. Compared with 1st-order noise-shaping loop, the residue voltage save capacitor of the 2nd-order noise-shaping loop consists of about 4 times larger. Then it cannot be compatible with multi-biomedical sensor integrated system including ExG, PCG, BioZ, etc.

19

Second, there is the charge sharing problem. When the residue voltage is saved after the digital conversion, the charge sharing is occurred between the capacitor of the main integrator and the residue voltage save capacitor, so the quality factor of the noise-shaping loop is decreased. The quality factor of an ideal noise-shaping loop is 1, but the quality factor of the previous noise-shaping LDC is 0.64 due to the charge sharing problem. Therefore, the effective noise-shaping performance is decreased.

Third, there is the design complexity of a pre-amplifier with a gain of 2. The previous noise-shaping LDC utilizes a pre-amplifier with a gain of 2 to increase the noise-shaping performance. However, the design of a pre-amplifier with an accurate gain of 2 is difficult due to mismatch, and it increases the design complexity.

Fourth, the previous noise-shaping LDC only reduces the quantization noise, but cannot reduce the noise of core amplifier.

Therefore, this thesis discusses the design, that reduces the quantization noise through a simple and small area noise-shaping loop without the charge sharing problem, and reduces the noise of the core amplifier through chopper-stabilization technique.

3.1.3 Improved noise shaping loop

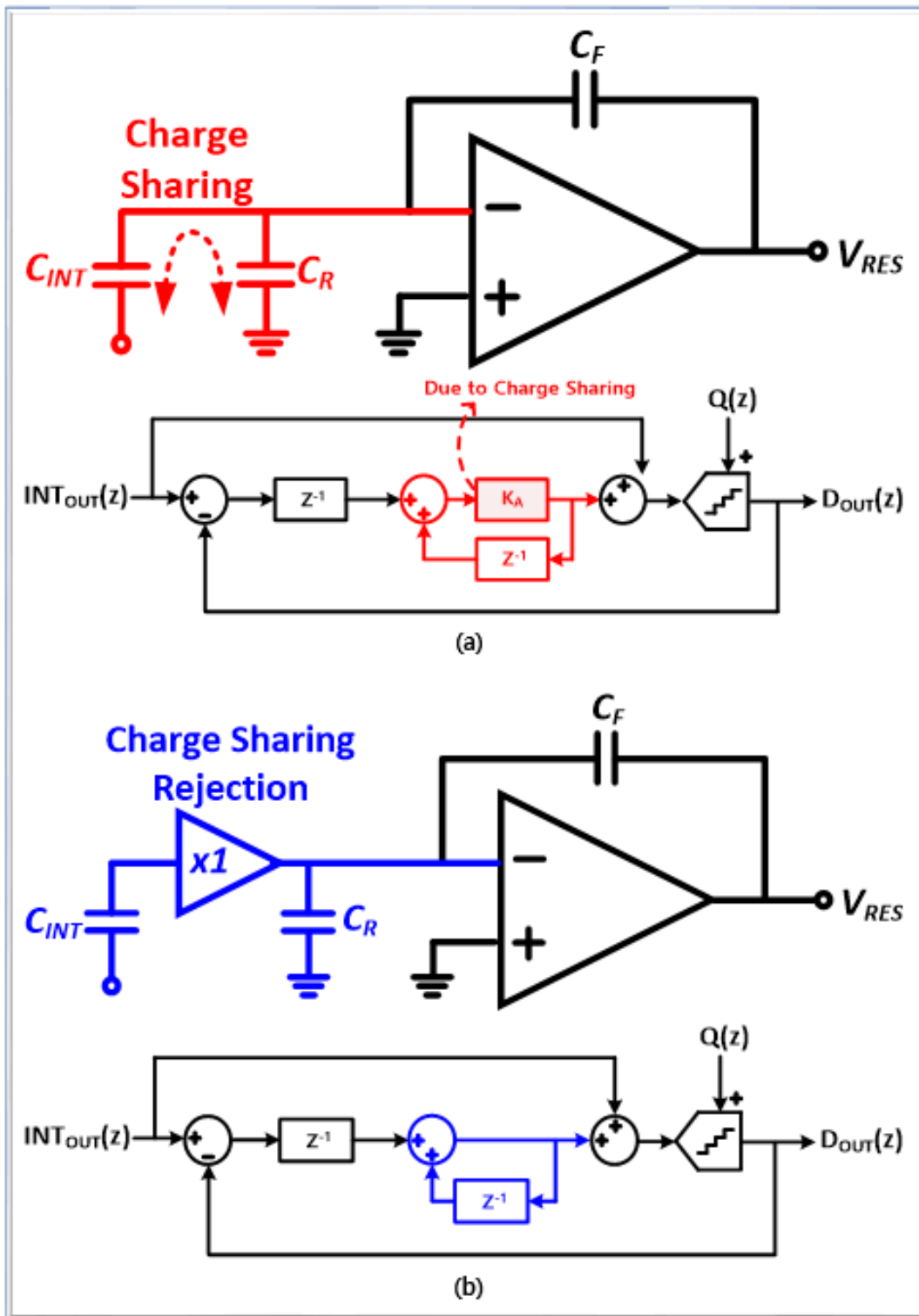Figure 3.7. Simplified depiction and equivalent signal flow diagram of the noise shaping dual-slope LDC (a) with charge sharing problem and (b) without charge sharing problem through charge sharing rejection buffer

21

Through the noise-shaping loop, the quantization noise is shaped from the low frequency region to the high frequency, but the kT/C noise contribution from the residue voltage save capacitor C_R of the noise-shaping loop is not shaped [17]. Hence, C_R should be sized enough, in order for kT/C noise from C_R not to degrade the total noise performance. But there are some problems, when C_R has large values. If C_R has large values, the main integrator cannot drive a large C_R for a short time, when a residue voltage is saved in C_R after digital conversion is finished. Consequently, an accurate value of a residue voltage is not saved in C_R, then it prevents the practical implementation of the noise-shaping loop. In addition, due to charge sharing between C_R and the capacitor C_{INT} of the main integrator, the effective noise-shaping performance of the noise-shaping loop is degraded.

To solve these issues, this thesis proposes the simple structure that rejects charge sharing to achieve high noise-shaping performance. As shown in figure 3.7.(a), when the simple noise-shaping loop is implemented, K_A is decreased by the charge sharing problem. The transfer function of the total system is shown in equation (3.8), and the noise transfer function is affected by the decreased K_A.

$$D_{OUT}(z) = INT_{OUT}(z) + (1 - K_A z^{-1})\, Q(z) \qquad (3.8)$$

On the other hand, as shown in figure 3.7.(b), the charge sharing problem can be solved by utilizing the charge sharing rejection buffer. The charge sharing rejection buffer helps the main integrator drive C_R. Also, the charge sharing can be cut-off by inserting a charge sharing rejection buffer between C_{INT} and C_R. Through this, the decrease of K_A can be prevented, as shown in equation (3.9).

$$D_{OUT}(z) = INT_{OUT}(z) + (1 - z^{-1})\, Q(z) \qquad (3.9)$$

Figure 3.8 shows the comparison of the noise transfer function with the charge sharing problem, without the charge sharing problem through the charge sharing rejection buffer, and that of the previous noise-shaping LDC. The red line is the plot of the noise transfer function with charge sharing problem, and in this design, the quality factor of 0.9. The blue line is without charge sharing problem through the proposed charge sharing rejection buffer. Comparing these two plots, it can be seen that the proposed structure prevents the degradation of noise-shaping performance by the charge sharing problem. The gray line is the plot of the noise transfer function of the previous noise-shaping LDC, and it shows that the proposed noise-shaping loop has similar noise-shaping performance to the previous noise shaping LDC, has a simple and small area design.

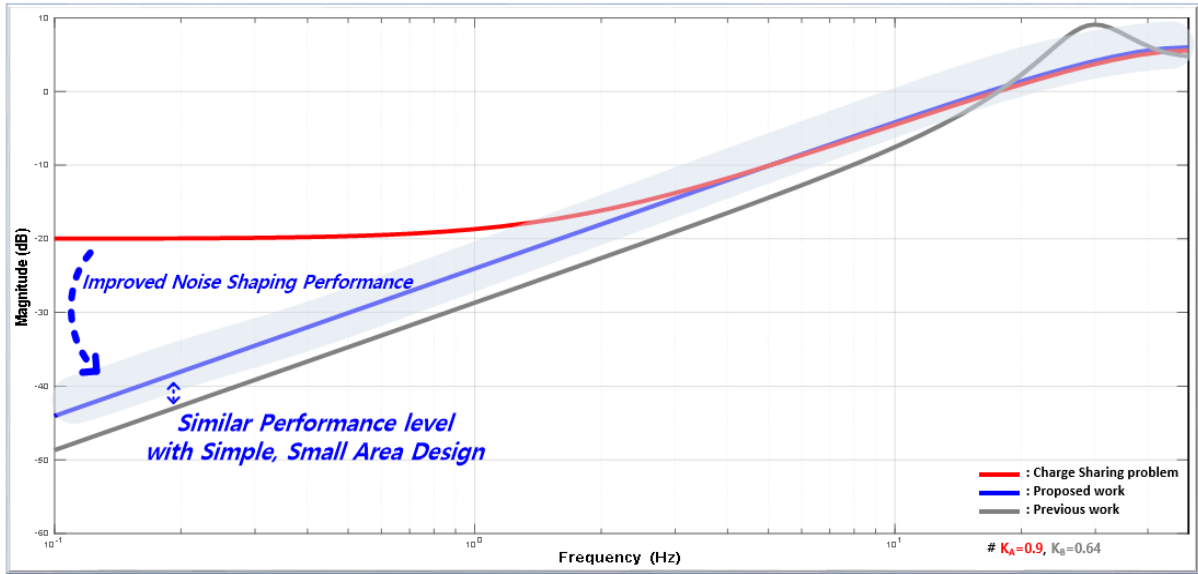Figure 3.8. Comparison of the noise transfer function with the charge sharing problem,
without the charge sharing problem through the charge sharing rejection buffer,
and that of the previous noise shaping dual-slope LDC
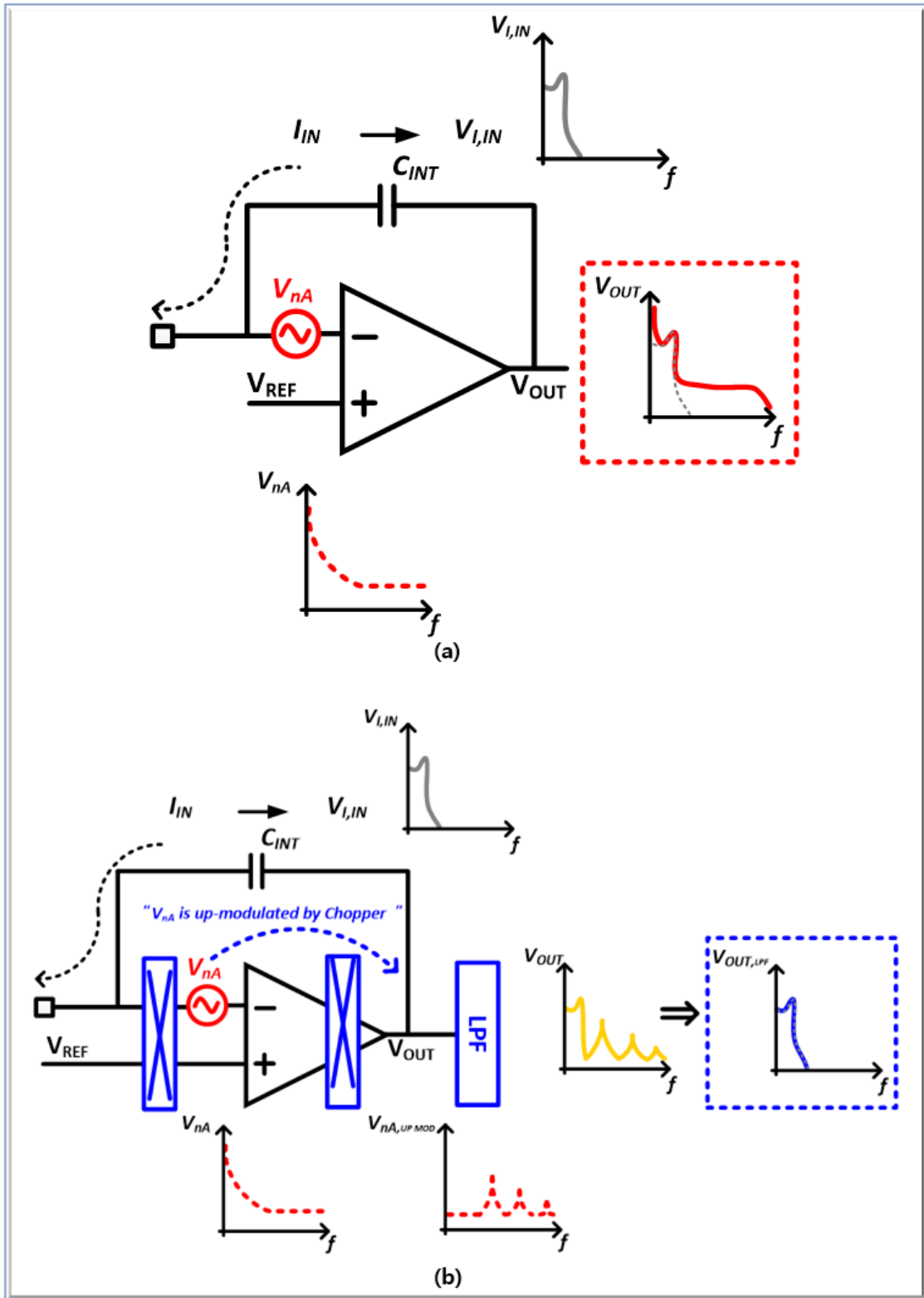
3.1.4 Chopper-stabilized dual-slope structure

Figure 3.9. Simplified schematic and frequency-domain illustration of the integrator with (a) simple and (b) chopper-stabilization technique in the dual-slope LDC

The noise of the core amplifier consists of the flicker noise and thermal noise. The thermal noise is Gaussian white noise, and this noise has a constant distribution of power over frequency. The flicker noise is 1/f noise, and as the term implies, this noise has a 1/f power spectral density. Then it has high noise power in the low frequency region, and overshadowed by thermal noise in the high frequency region. Meanwhile, the PPG signal has a bandwidth below 10Hz, which is a very low frequency region. Therefore, the total in-band noise performance of the proposed LDC is limited by the combination of flicker noise and thermal noise. Figure 3.9.(a) shows the simplified schematic and frequency-domain illustration, that the noise of the core amplifier distorts the in-band PPG signal.

Generally, bio-signals are in the low frequency region, then chopper-stabilization technique is adopted to remove 1/f noise and DC offset of the amplifier widely distributed in the low frequency region. The basic operation of chopper-stabilization technique is as follows [18]. First, the signal is modulated to the high frequency by passing through the chopper, and the noise of amplifier such as 1/f noise and DC offset remains in the low frequency region. And the combination of the modulated signal and noise is amplified. To the next, it passes through the chopper once again, then the noise is up-modulated to high frequency and the signal is demodulated to low frequency. Finally, only the clearly amplified signal remains and the noise is cut-off, after passing through the low-pass filter (LPF).

The chopper-stabilization technique in the dual-slope LDC is performed similarly, as shown in figure 3.9.(b). The input PPG signal I_{IN} is integrated into $V_{I,IN}$ through the integrator, and the noise of the core amplifier is up-modulated to the high frequency by passing through the chopper. Unlike general chopper-stabilization technique, the input signal is not modulated in the dual-slope LDC, but the input chopper of the integrator maintains negative-feedback during chopping operation. Likewise, only a noiseless signal remains, after passing through LPF. And the operation of the counter has inherent LPF characteristic.

As a results, the noise of the core amplifier is removed by filtering out the up-modulated noise through chopper-stabilization technique.

3.1.5 DEM method for current DAC
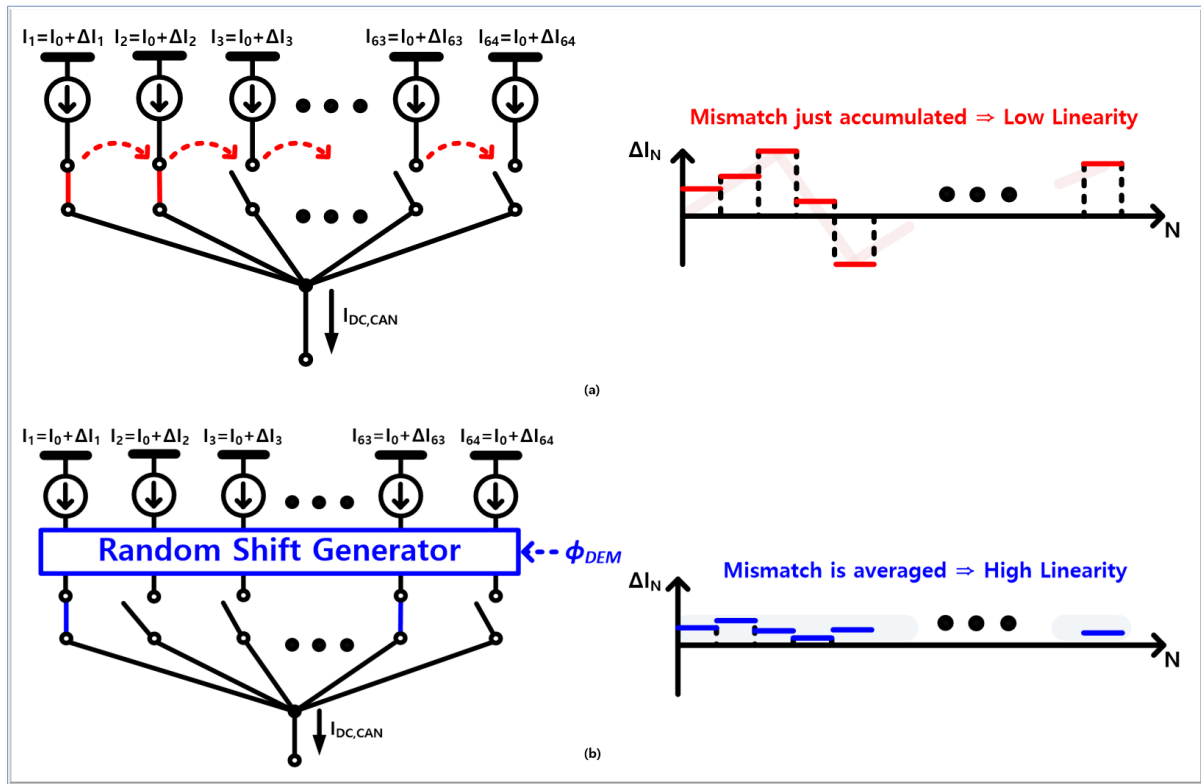
Figure 3.10. Simplified structure and mismatch of DC cancellation current DAC (a) without and (b) with DEM method

To achieve a high dynamic range, the proposed LDC utilizes DC cancellation current ($I_{DC,CAN}$) digital-to analog converter(DAC) to cancel the large DC baseline of the PPG signal. $I_{DC,CAN}$ consists of parallel unit current cell, and controlled by D_{DC} fed back through up/down counter. Due to the mismatch on a chip fabrication process, each unit current cell has a different current value. As a results, accurate PPG waveform cannot be obtained due to linearity problem caused by $I_{DC,CAN}$. Figure 3.10.(a) shows the simplified structure and mismatch of a simple $I_{DC,CAN}$ without dynamic element matching(DEM) method. In a simple $I_{DC,CAN}$, the unit current cells are turned on in order. Therefore, the current mismatch value is different according to each D_{DC}, so the LDC has low linearity. On the other hand, if the DEM method is applied as shown in figure 3.10.(b) [19], with the operation of random shift generator, different unit current cells are turned on in each sampling period, in the same D_{DC}. Through this operation, the mismatch of each unit current cell becomes averaged, then the LDC has high linearity.

3.2 Proposed dual peak detector for PCG

3.2.1 Conventional peak detector
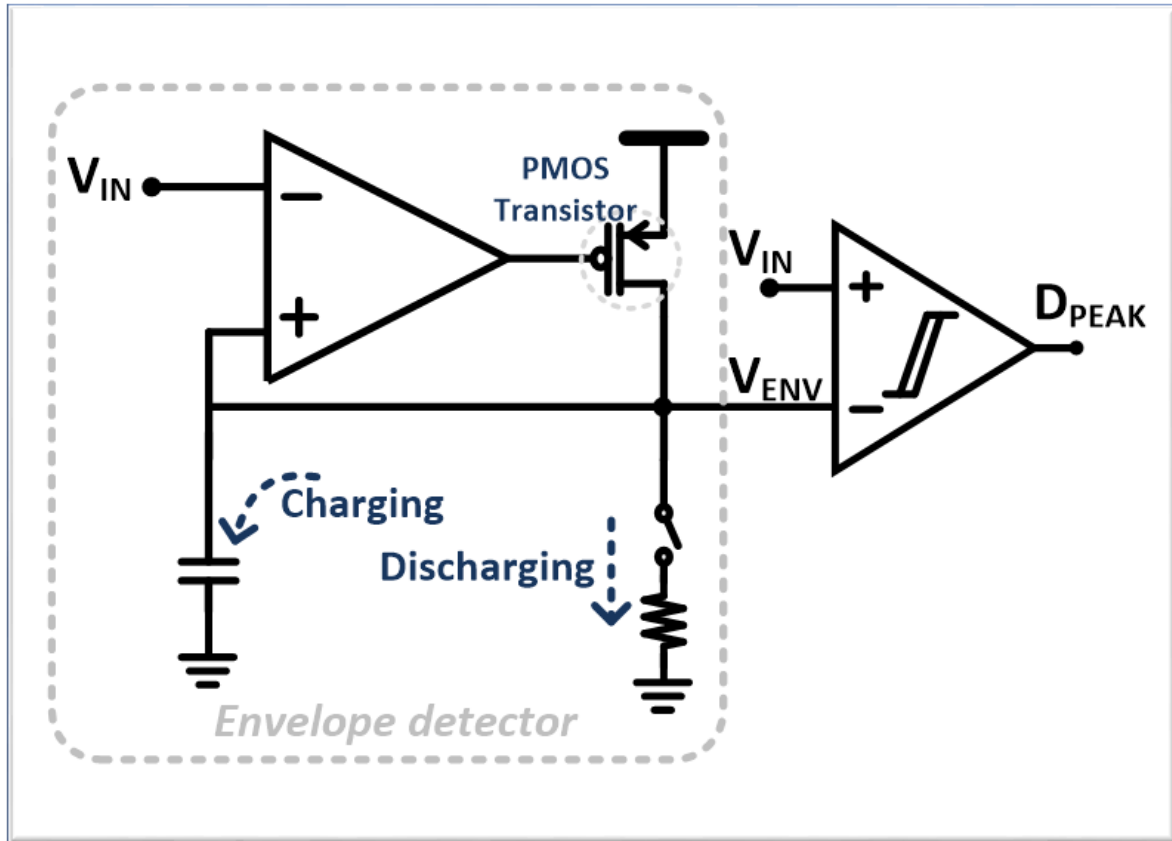
Figure 3.11. Schematic of a conventional analog peak detector

For VTT-based blood pressure estimation, VTT and ET are required. To calculate VTT, the PCG S1 peak is needed. And, to calculate ET, the PCG S1 peak and PCG S2 peak are needed. Therefore, in order to measure blood pressure with the proposed estimation method, both the PCG S1 peak and the PCG S2 peak should be detected. In general, in order to recognize the peak of the signal, DSP is performed in the MCU after an analog signal is converted into digital data through an ADC. However, this process requires the transmission of the entire signal waveform to the MCU, which is the relatively big data communication, and the MCU must perform complex signal processing. As a results, power consumption and processing burden of the MCU increase.

To solve this issue, a peak detector has been developed to detect the peak of analog signal. The structure of a conventional analog peak detector is shown in figure 3.11 [20], and its operation consists of a charging phase and a discharging phase determined by comparing the input signal (V_{IN}) with the output of the envelope detector (V_{ENV}). In a discharging phase, $V_{IN} < V_{ENV}$, the PMOS

transistor is turned off and only the capacitor is discharged, so V_{ENV} decreases slowly. In a charging phase, $V_{IN} > V_{ENV}$, the PMOS transistor is turned on and the capacitor is charged until V_{ENV} follows V_{IN}. The peak detector recognizes this point as the peak of V_{IN}, and it detects the peak of the signal quite accurately, although there is a slight error in the peak detection results.
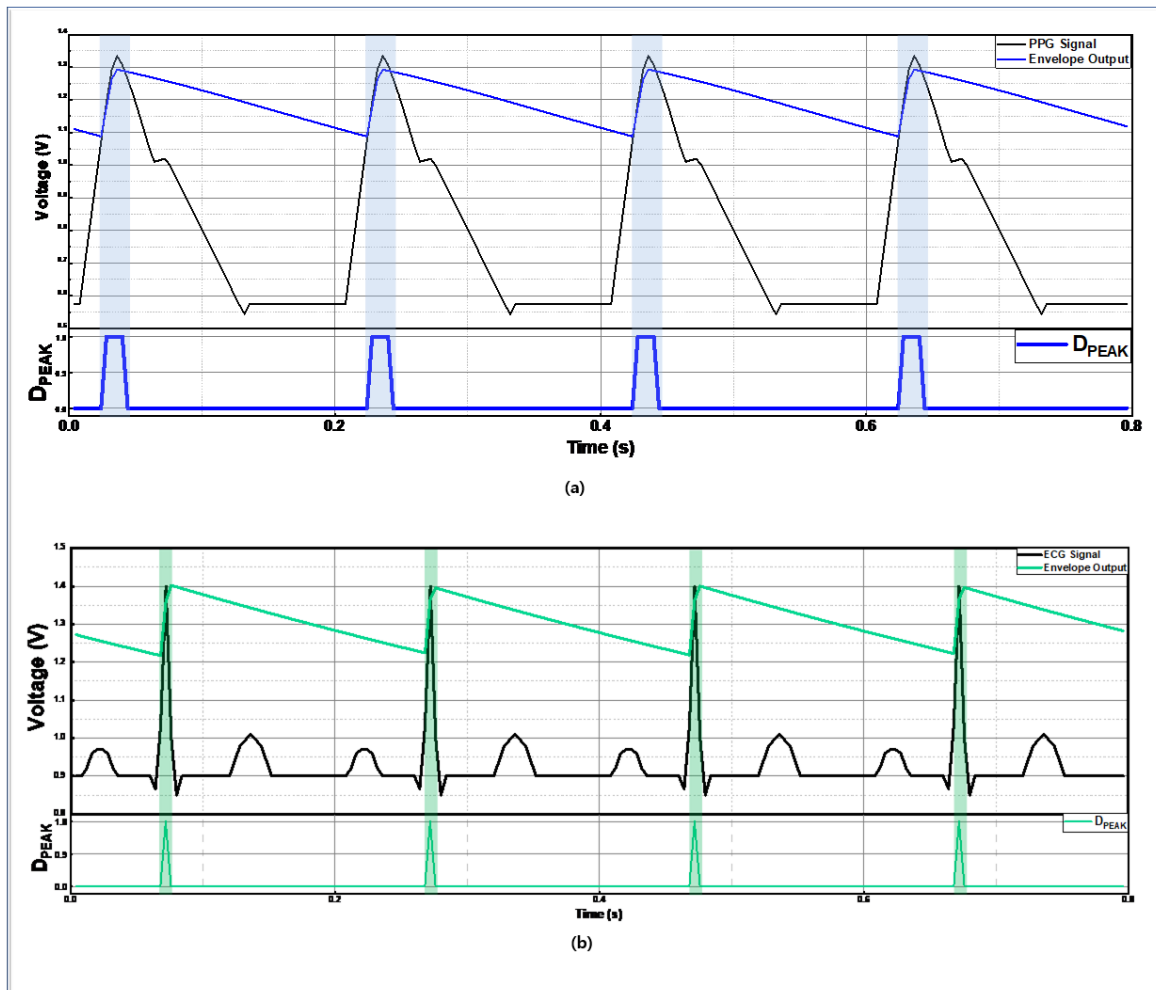
Figure 3.12. Peak detection simulation results of (a) PPG signal by TIA and (b) ECG signal through a conventional peak detector

Figure 3.12. shows the peak detection results of (a) ECG signal and (b) PPG signal by TIA through a conventional peak detector. A conventional peak detector is suitable when there is only one peak per sample, like a PPG signal. Or, like an ECG signal, when the R peak you want to find is clearly larger than the P peak and T peak, it is suitable because the envelope detector can track only the R peak.

However, a conventional peak detector is not suitable in the PCG signal, because PCG peaks cannot be detected properly. For example, as shown in figure 3.13.(a), if a conventional peak detector that consist of the envelop detector with a slow discharging speed is used, one of the PCG S1 peak or the

PCG S2 peak is missed, and only one other can be detected. Conversely, as shown in figure 3.13.(b), if the one with a fast discharging speed is used, both the PCG S1 peak and the PCG S2 peak are detected, but they cannot be distinguished, so two different peaks are shown as two identical peaks. For this reason, a new peak detector should be developed that can detect both the PCG S1 peak and the PCG S2 peak, and distinguish the two peaks from each other.

Figure 3.13. Results of peak detection of the PCG signal through a conventional peak detector, (a) one peak is missed or (b) two peaks are not distinguished

29

3.2.2 Dual peak detector to distinguish different PCG peaks

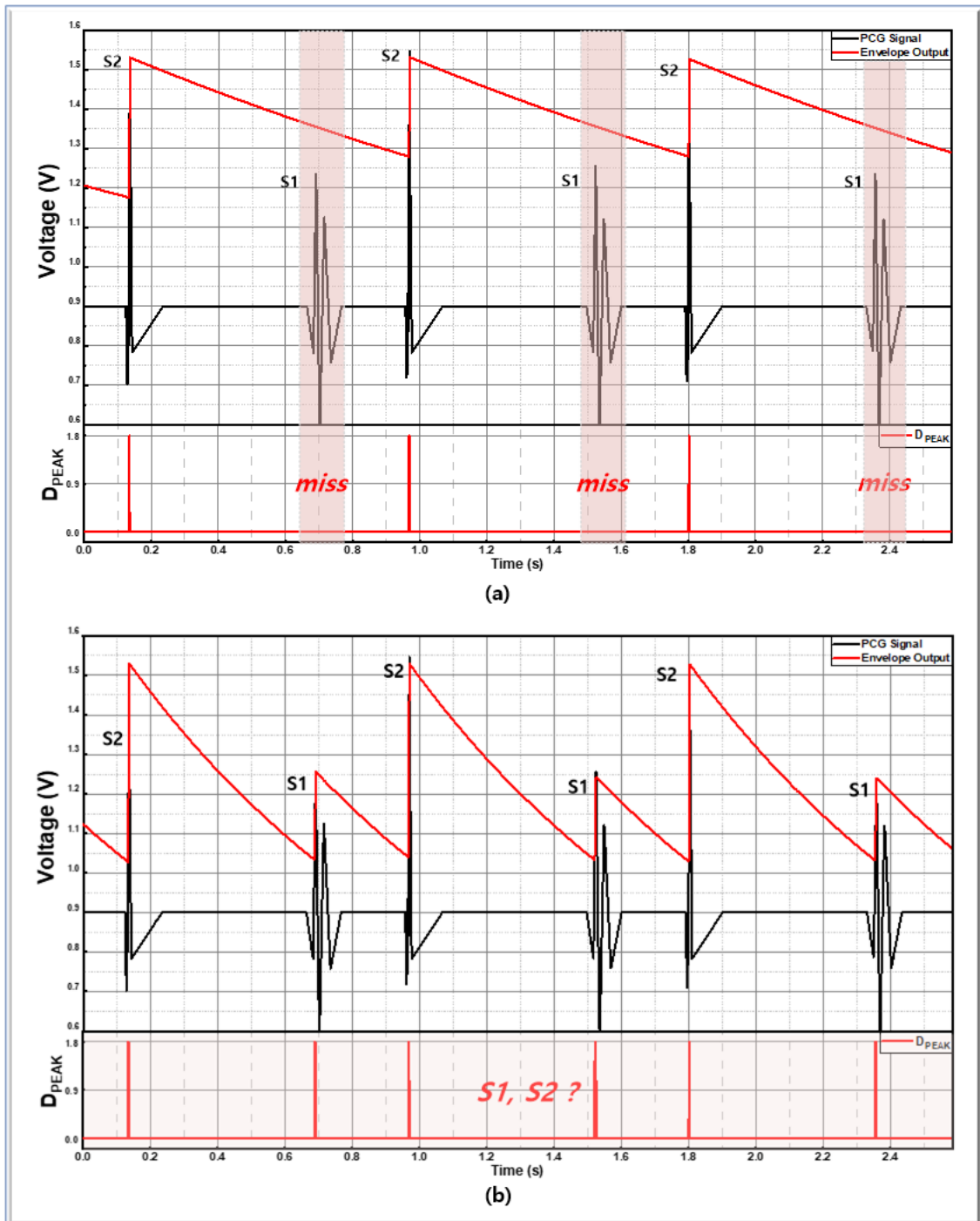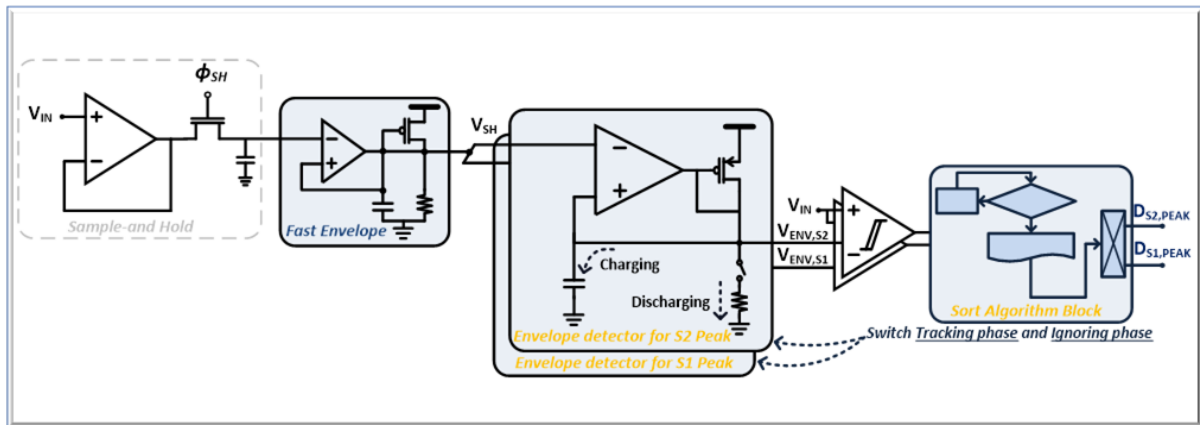

Figure 3.14. Schematic of the proposed dual peak detector

Figure 3.14 shows the circuit structure of the proposed dual peak detector. The proposed dual peak detector consists of a fast envelope detector to avoid murmur noise, parallel envelope detectors for each PCG S1 peak and PCG S2 peak, and sort algorithm block to distinguish between the PCG S1 peak and the PCG S2 peak. Because two types of peaks are detected in one PCG signal, the two envelope detectors for each peak share one sample-and hold circuit and a fast envelope detector. The PCG AFE consists of CCIA and PGA, then sample-and hold operation (ϕ_{SH}) is synchronized with the PCG AFE operation. The output of the sample-and hold circuit is connected to the input of fast envelope detector. The PCG signal has murmur noise, the pre-envelope with a fast discharging speed helps to avoid being affected by murmur noise. Thereafter, the pre-enveloped signal becomes an input of parallel envelope detectors, and the operation of each envelope detector consists of a charging phase and a discharging phase, same with a conventional envelope detector. The discharging speed of the envelope detector in the analog peak detector is controlled by the operating frequency of duty-cycled resistor and the size of the charged capacitor, and the smaller the size of the charging capacitor and the faster the operating frequency of the duty-cycled resistor, the faster the discharging speed of it is. On the other way, the larger the size of the charging capacitor and the slower the operating frequency of the duty-cycled resistor, the slower the discharging speed of it is. Also, the discharging speed of each envelope detector in the proposed dual peak detector is controlled independently, and each one can be set according to the amplitude of the PCG S1 peak and the PCG S2 peak. Sort algorithm block makes the two envelope detectors alternately operate between tracking phase and ignoring phase, and distinguishes the output of each comparator into the PCG S1 peak and the PCG S2 peak. If the envelope detector is in tracking phase, when $V_{IN} > V_{ENV}$, the envelope detector tracks the input signal, and the output of the comparator is detected. Conversely, if the envelope detector is

in ignoring phase, even when $V_{IN} > V_{ENV}$, the envelope detector does not track the input signal then keeps discharging operation, and the output of the comparator is discarded. Therefore, by switching tracking phase and ignoring phase of the envelope detector, each envelope detector is triggered on only one type of peak.
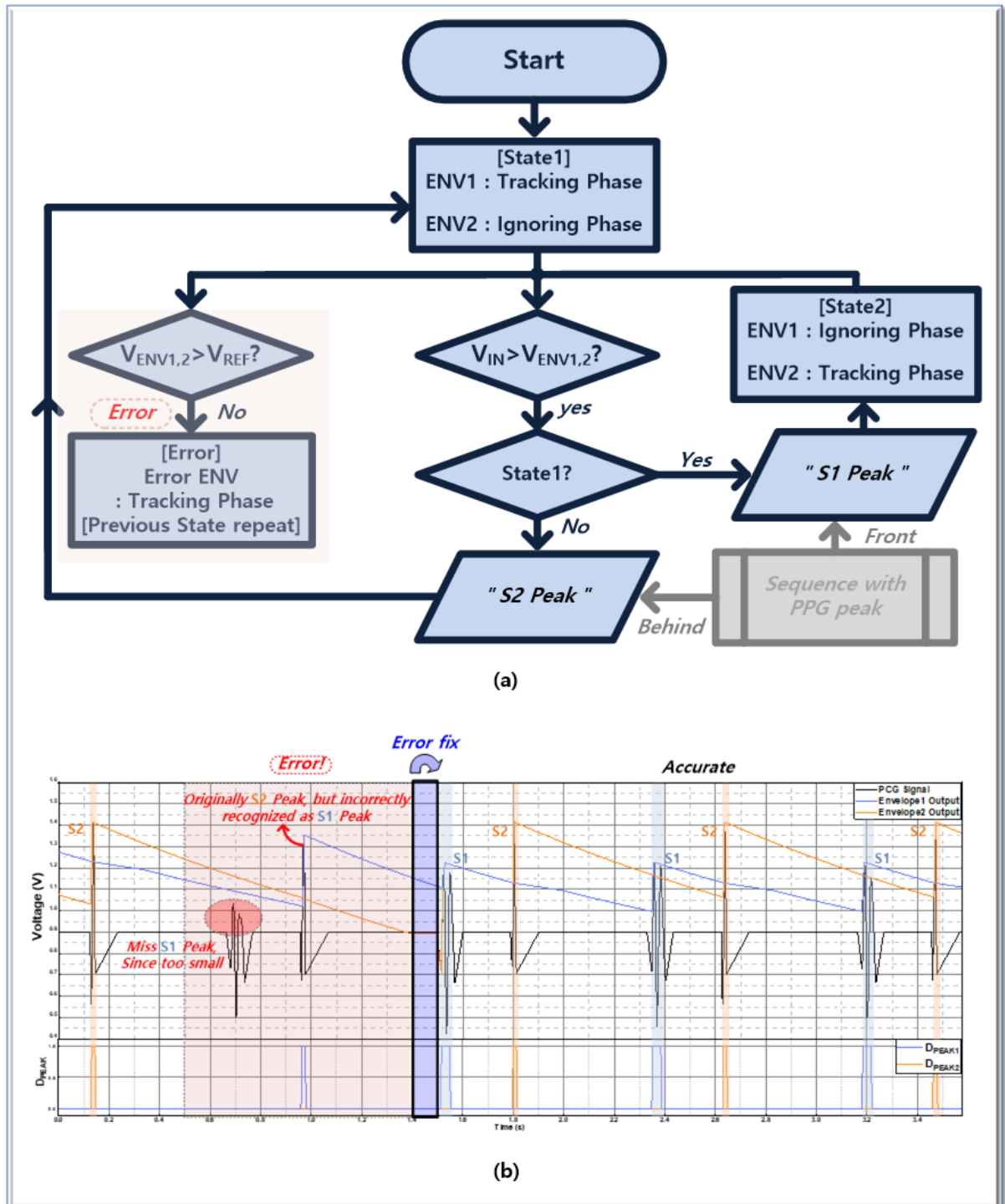

Figure 3.15. (a) Flow chart and (b) simulation results of sort algorithm block with self-error fix function in the proposed dual peak detector

Figure 3.15.(a) shows a flow chart of sort algorithm block in the proposed dual peak detector. First, in the initial state, the PPG peak is utilized to determine whether it is an envelope detector for the PCG S1 peak or the PCG S2 peak. The PCG S1 peak is in front of the PPG peak and the PCG S2 peak is behind of the PPG peak, so based on this relationship, the envelope detectors are sorted by the initial output of each envelope detector and the PPG peak. Sequences with the PPG peak are only utilized in the initial sort of the envelope detector. After that, when the envelope detector is triggered with $V_{IN} > V_{ENV1,2}$, each envelope detector operates alternately between tracking phase and ignoring phase, by switching between state1 and state2. The PCG S1 peak and PCG S2 peak are distinguished based on this state. Meanwhile, as shown in figure 3.15.(b), if a specific peak is too small, the peak detection by this switching method makes an error. To solve this problem, the self-error fix function is added, that compares the output of the envelope detector with the reference voltage and corrects it to an accurate state. The self-error fix function is turned on when $V_{REF} > V_{ENV1,2}$, and the envelope detector which is in error state, follows V_{IN}. Also, the state for peak detection keeps on the previous state. By this function, it is possible to correct the error peak detection state to accurate when the next peak is detected. Therefore, through the proposed dual peak detector, the PCG S1 peak and PCG S2 peak can be accurately distinguished and detected.

Chapter IV
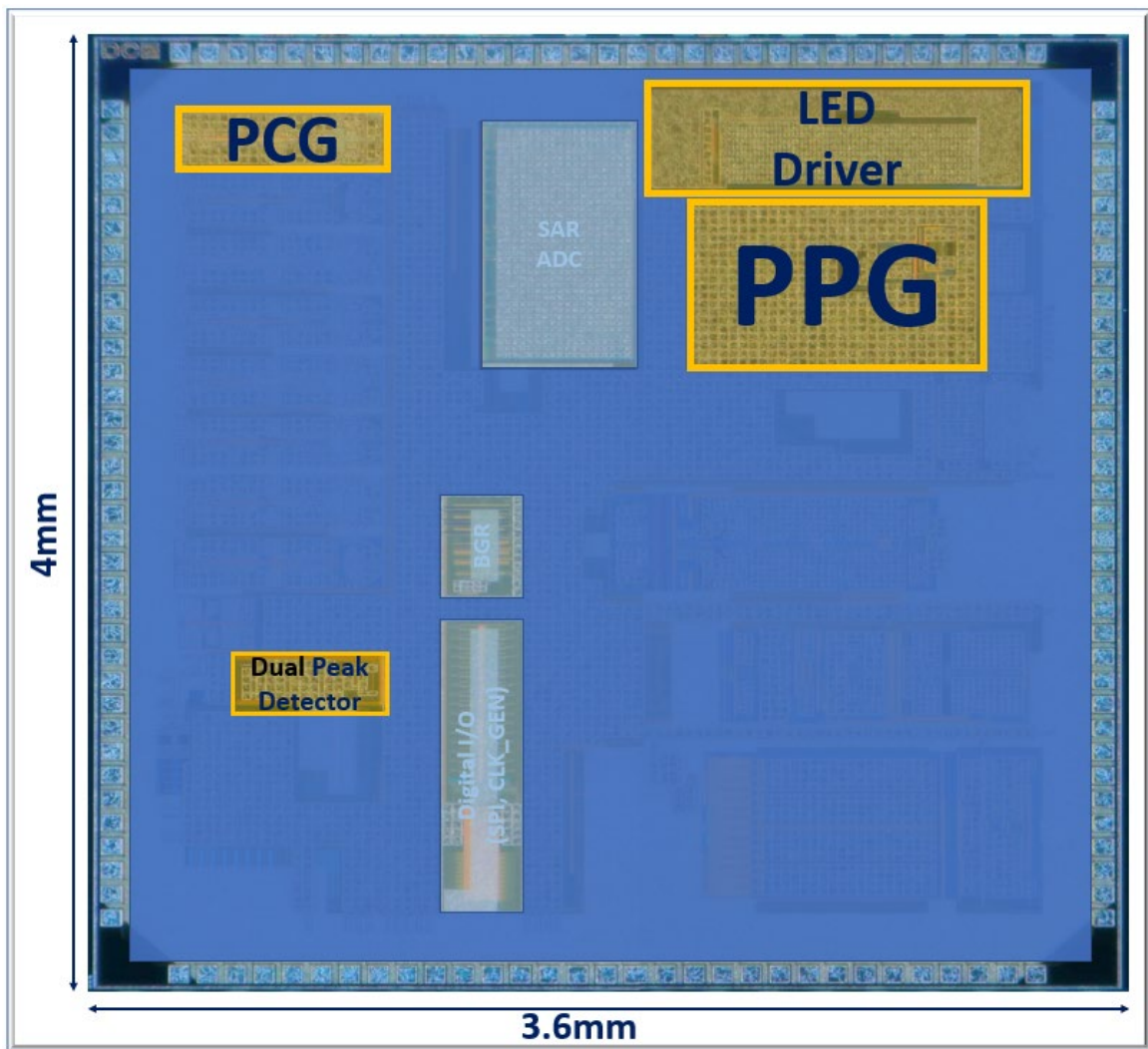
Experimental Result

Figure 4.1. Chip photographs of the designed ROIC

This chapter described the experimental results of the PPG ROIC and PCG ROIC proposed in previous chapter. Also, the system implementation with the designed ROIC is shown. Figure 4.1 is the chip photographs of the designed ROIC. This chip is fabricated in TSMC 0.18μm BCD process, and

has a total chip die area of 14.4mm^2. The area of each core block is as follows: PPG ROIC is 0.717mm^2, LED driver is 0.467mm^2, PCG AFE is 0.183mm^2, and peak detector is 0.07mm^2. Due to heat dissipation of LED driver, it should be designed large enough. The miniaturized prototype sensor module is implemented, which has the size of 3.5 cm x 7.4 cm. The photograph of both sides of the developed prototype sensor module and diaphragm substrate is shown in figure 4.2.
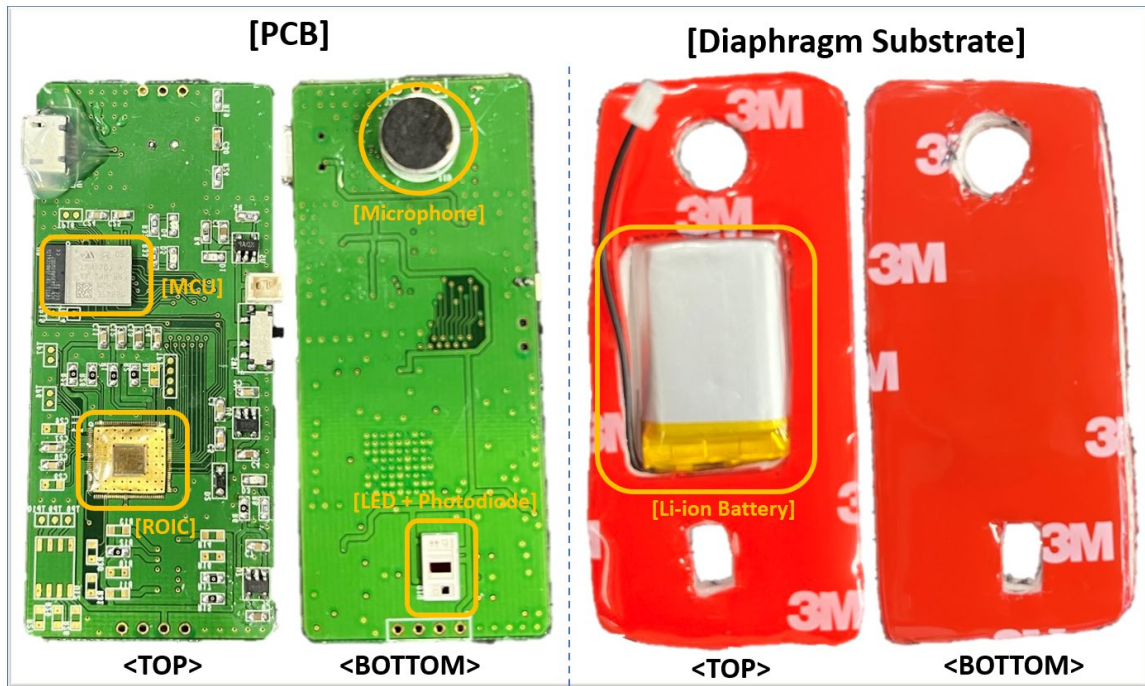
Figure 4.2. Photographs of both sides of the developed prototype sensor module
and diaphragm substrate

To collect heart beat sound without cumbersome stethoscope, the diaphragm substrate is located below the PCB substrate. There is a hole in the center of the diaphragm substrate to allow the battery to be inserted inside it, which is the area-efficient way to place the battery. The top side of the prototype sensor module is composed of MCU, ROIC, and other component parts. And the bottom side is composed of a condenser microphone and PPG sensor, which consists of various types of LEDs and photodiode, together. Therefore, the photodiode and LED for PPG, a condenser microphone for PCG, ROIC, and MCU are integrated in a single PCB substrate.
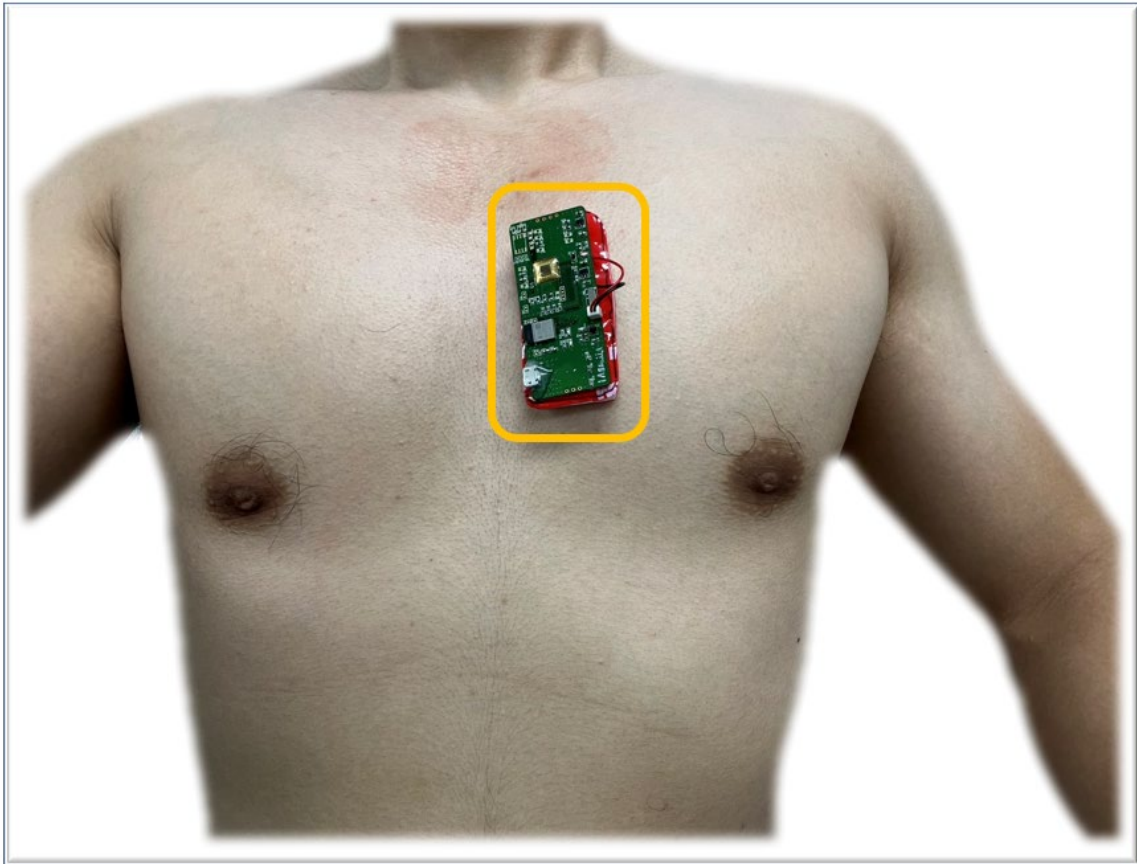
Figure 4.3. Measurement position of the proposed health monitoring system

Figure 4.3 shows the measurement position of the proposed health monitoring system. Since the heart is skewed to the left, the prototype sensor module is slightly placed on the left side of the chest for the effective signal measurement. Thanks to a miniaturized size and all-in-one composition, the proposed system can be applied to wearable device and suitable for comfortable use in daily life.

4.1 Measurement results of the proposed LDC

For the chest PPG readout, a low-noise PPG ROIC is needed. As described in chapter 3.1, the two dominant noise sources of a conventional dual-slope LDC are the noise of the core amplifier and the quantization noise. First, the noise of the core amplifier can be reduced by chopper-stabilization technique. Figure 4.4 shows the noise spectral density of the proposed dual-slope LDC with and without chopper-stabilization technique. The sampling frequency is 125Hz. Thanks to the chopper-stabilization technique the in-band(0.1~50Hz) integrated noise is reduced from $2.89nA_{rms}$ to $1.82nA_{rms}$, which means the noise suppression of 4.01dB.
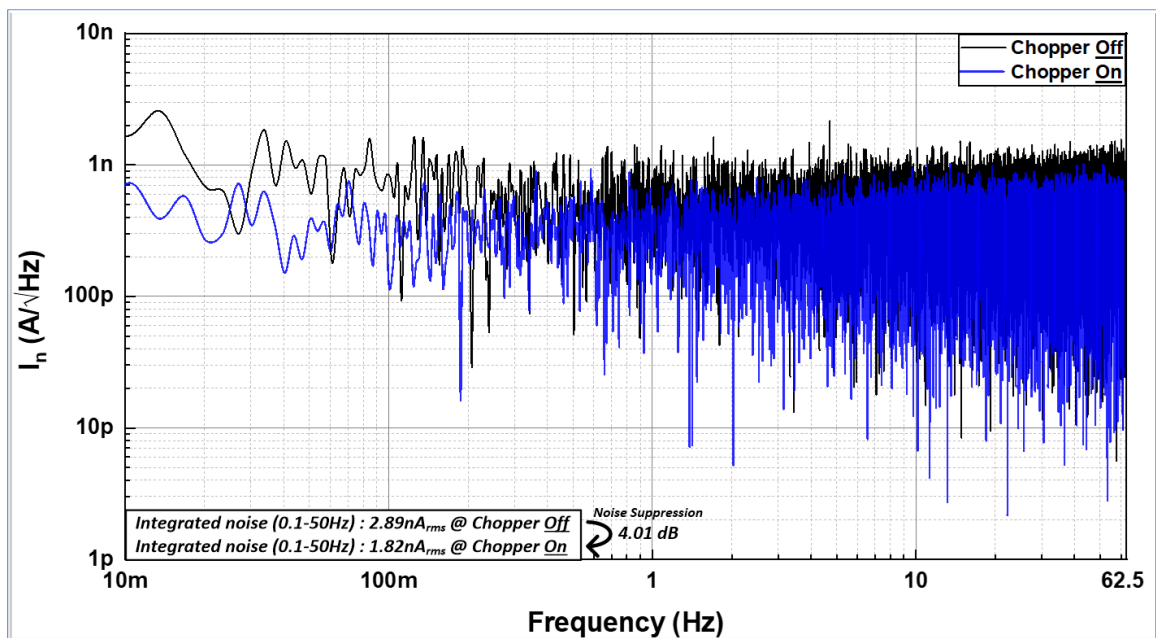
Figure 4.4. Noise spectral density of the proposed dual-slope LDC w/wo chopper-stabilization technique

Second, the quantization noise can be reduced by the noise-shaping loop. Figure 4.5 shows the noise spectral density of the proposed dual-slope LDC according to noise-shaping loop and with and without chopper-stabilization technique. The sampling frequency is 2kHz, which is the OSR of 16. As shown in the figure, with the simple noise-shaping loop, the integrated noise is reduced from $2.88nA_{rms}$ to $1.41nA_{rms}$, which means the noise suppression of 6.2dB. However, with the improved noise-shaping loop, the charge sharing problem can be solved, and the noise-shaping performance is improved.

So, the integrated noise is reduced to 833pA$_{rms}$, which means the noise suppression of 10.7dB. And further noise suppression is possible with chopper-stabilization technique, then the integrated noise is reduced up to 668pA$_{rms}$, which means the noise suppression of 12.7dB.
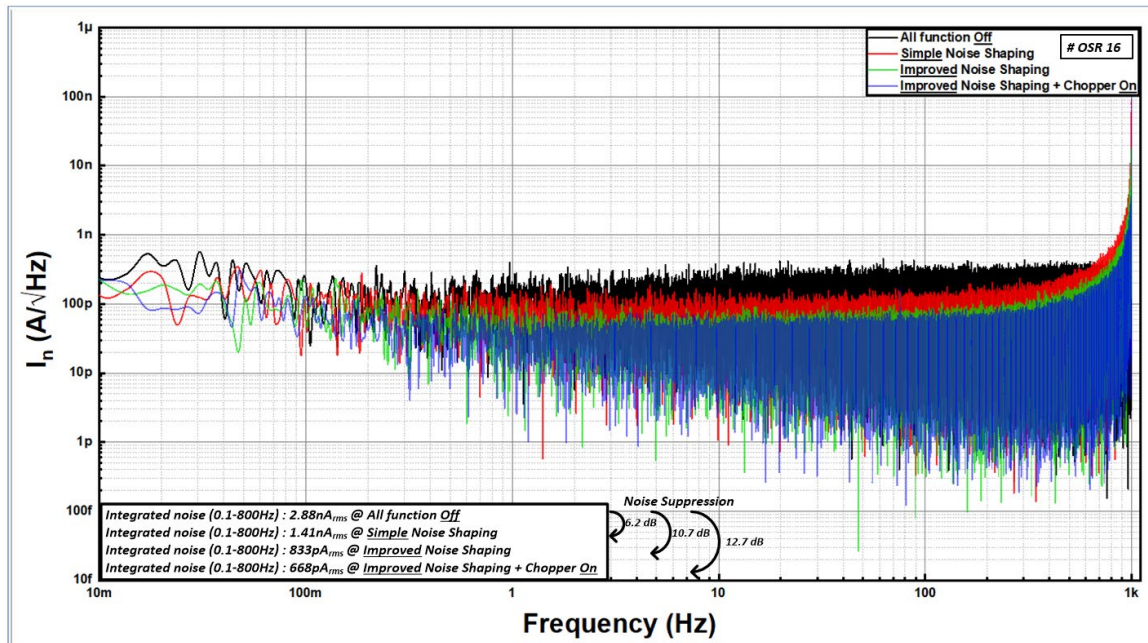

Figure 4.5. Noise spectral density of the proposed dual-slope LDC according to noise-shaping loop and w/wo chopper-stabilization technique

Figure 4.6 shows the comparison of the noise performance plot between the conventional dual-slope LDC and the proposed dual-slope LDC. With the decimation filter, the sampling frequency is lower from 2 kHz back to 125 Hz, and the shaped high frequency noise is cut-off. Therefore, compared to the conventional dual-slope LDC without noise-shaping loop and chopper-stabilization technique, the integrated noise of the proposed dual-slope LDC is reduced from 2.89nA$_{rms}$ to 407pA$_{rms}$, which means the noise suppression of 17dB.

Consequently, thanks to improved noise-shaping loop and chopper-stabilization technique, the noise performance of the proposed dual-slope LDC is dramatically improved. As a results, the PPG measurement on the chest is possible.
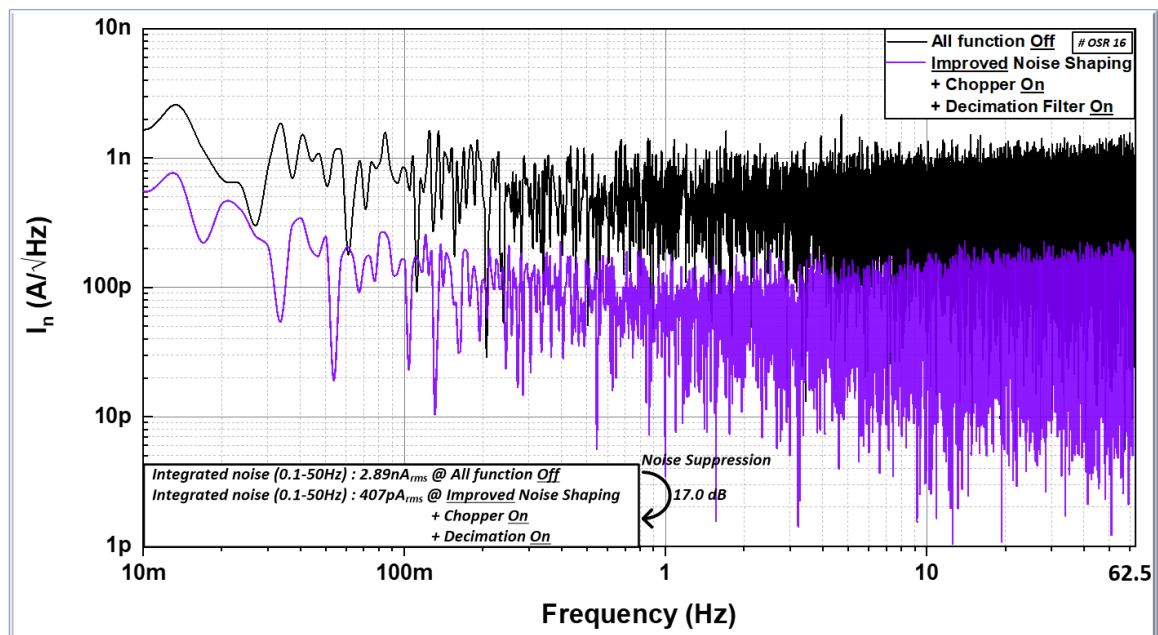
Figure 4.6. Comparison of noise performance plot between a conventional dual-slope LDC and the proposed dual-slope LDC

Figure 4.7 shows a signal-to-noise ratio and dynamic range of the proposed dual-slope LDC. By utilizing 6bit DC cancellation current DAC, the maximum input current up to 288μA can be applied. And in this case, the maximum SNR of 92.7dB is achieved. The dynamic range, which is the ratio between the achievable maximum input current and the achievable minimum integrated noise, is 116.9dB. As mentioned in chapter 2.1, the PPG signal is a small AC component superimposed on a large DC component. And the value of this DC component varies greatly depending on the measurement position. Hence, thanks to wide dynamic range, the proposed PPG ROIC can measure PPG signal in various body parts.
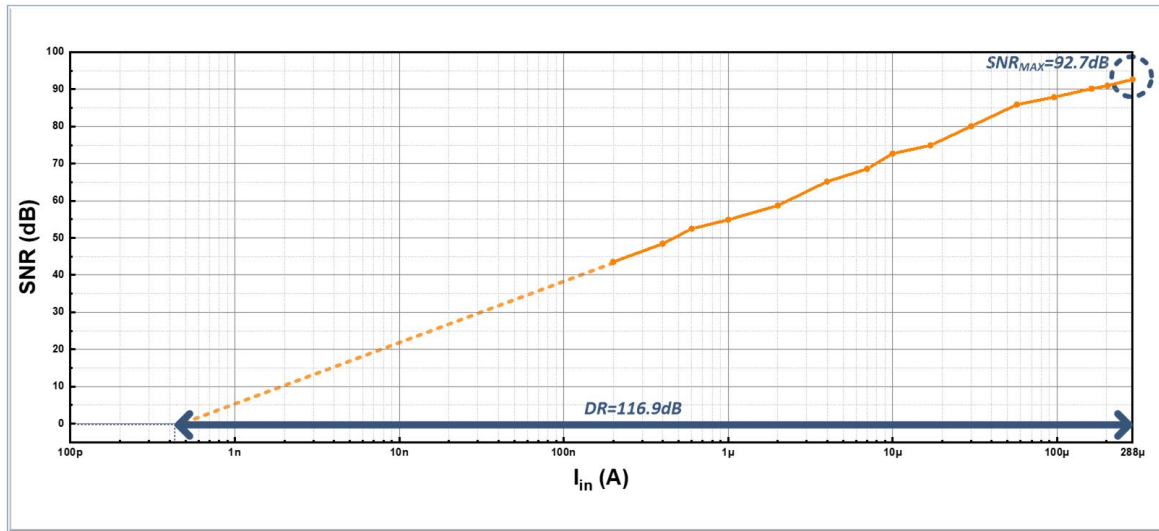
Figure 4.7. Signal-to-noise ratio and dynamic range of the proposed dual-slope LDC
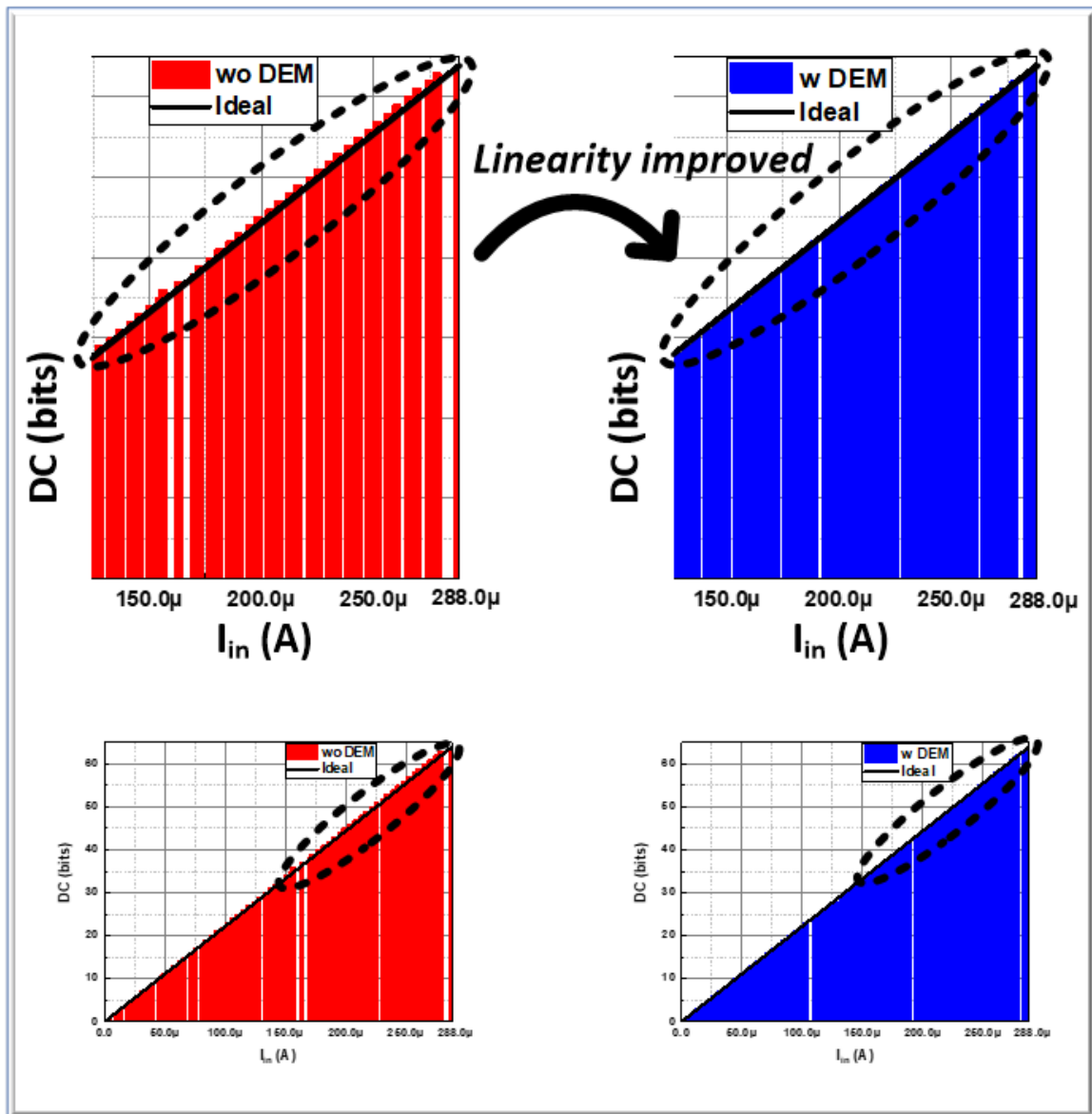
Figure 4.8. Comparison of linearity improvement of DC cancellation current DAC w/wo DEM

Thanks to DC cancellation current DAC, a wide dynamic range is achieved. However, as described in chapter 3.1.6, each unit current cell of DC cancellation current DAC has an inherent mismatch. And this mismatch causes linearity problem. Thus, the DEM method is applied. Figure 4.8 shows the comparison of the linearity improvement of DC cancellation current DAC with and without the DEM method. As shown in the figure, without the DEM method, the DC bit according to the input current has a non-linear characteristic, which means the LDC has a linearity problem. But, with the DEM method, the mismatch is averaged, and the linearity of the proposed LDC is improved. Consequently, thanks to the DEM method, accurate PPG signal measurement in various body parts is possible with high linearity.

4.2 Measurement results of the proposed dual peak detector

For VTT-based blood pressure estimation, the two PCG peaks should be distinguished. As explained in chapter 3.2, for the peak detection of two different peaks through the MCU, the relatively big data is transmitted from ROIC to MCU, and the complex digital signal processing is performed in the MCU. For such communication and processing, a high performance MCU is required which can be operated at high-speed. However, in the reference [21], it is explained that the power consumption of the MCU increases, when the operating frequency is high. Also, since the distinction process at the MCU is quite complex, the processing burden is increased. In order to solve this problem, as described in the chapter 3, the dual peak detector is introduced for the PCG channel.
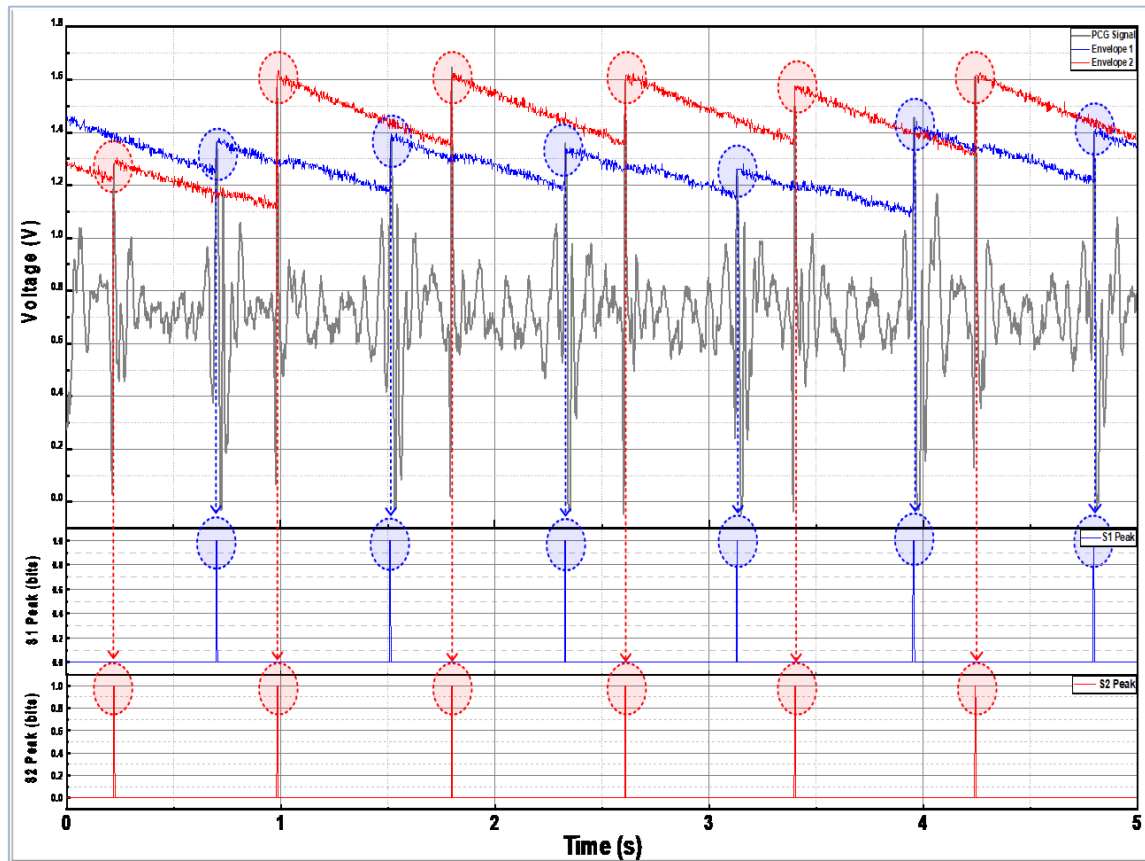
Figure 4.9. Results of the proposed dual peak detector with waveforms of two envelope detectors for each PCG peak

41

Figure 4.9 shows the results of the proposed dual peak detector with waveforms of two envelope detectors for each PCG peak. The signal from a condenser microphone is amplified through the PCG AFE, and then through the fast envelope detector, the envelope of the PCG signal without the murmur noise is acquired. Thereafter, by switching alternately between tracking phase and ignoring phase, the two different peaks of the PCG signal can be detected. Furthermore, the PCG S1 peak and PCG S2 peak can be distinguished with the proposed dual peak detector.

Therefore, with the proposed dual peak detector for PCG channel, the power consumption and processing burden of the MCU decrease. As a results, it is suitable for a low-power consumption application for long-term operation.

4.3 Blood pressure estimation with health monitoring system on the chest

4.3.1 Blood pressure estimation with VTT
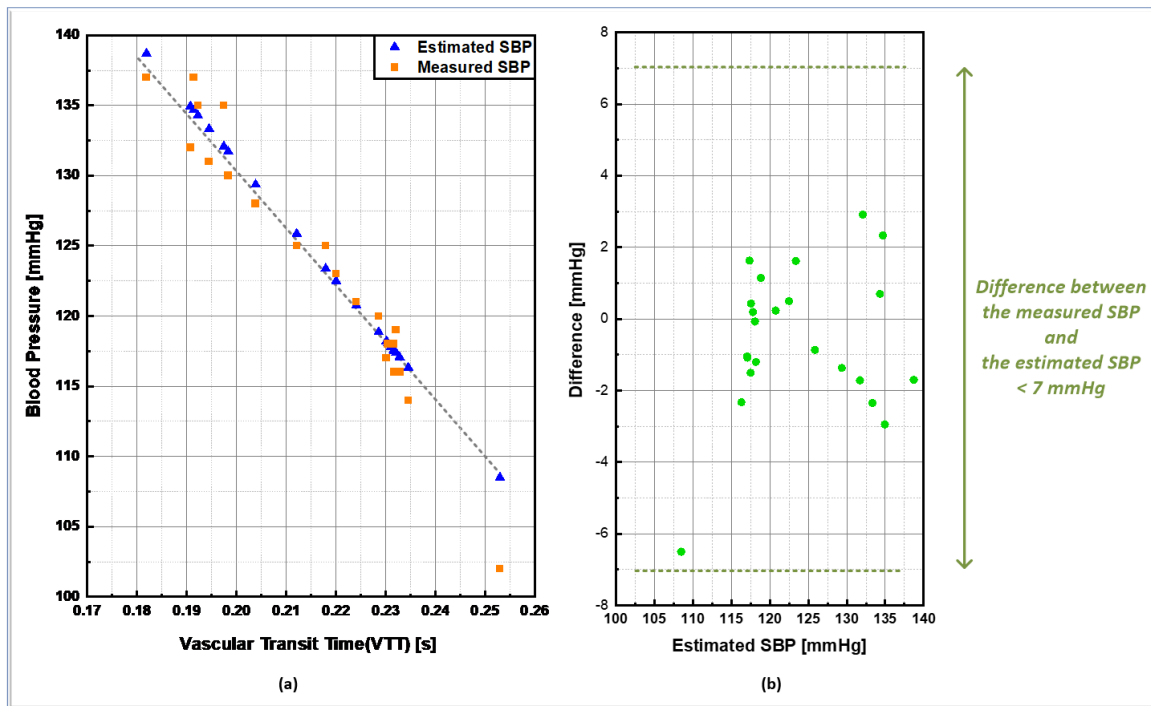
Figure 4.10. (a) The trend of the systolic blood pressure change as a function of vascular transit
time change and (b) difference between estimated SBP and measured SBP

As described in the chapter 2.3.2, the blood pressure is inversely related to VTT. Figure 4.10.(a) shows the trend of the systolic blood pressure change as a function of vascular transit time change. In order to find out the relationship between various blood pressure levels and VTT, the measurement is conducted under various conditions, such as taking a rest or after exercise. And as shown in the figure, when the blood pressure is high, VTT is shorter, and when the blood pressure is low, VTT is longer. The estimated blood pressure is calculated from the equation (2.1). To verify the accuracy of the estimated blood pressure, the measured blood pressure is acquired from the commercial blood pressure gauge, together. The difference between the measured blood pressure and the estimated blood pressure is shown in figure 4.10.(b). And the difference between them does not exceed a 7mmHg. Therefore, this VTT-based blood pressure monitoring system estimates blood pressure well.

4.3.2 Multi-mode health monitoring system on the chest
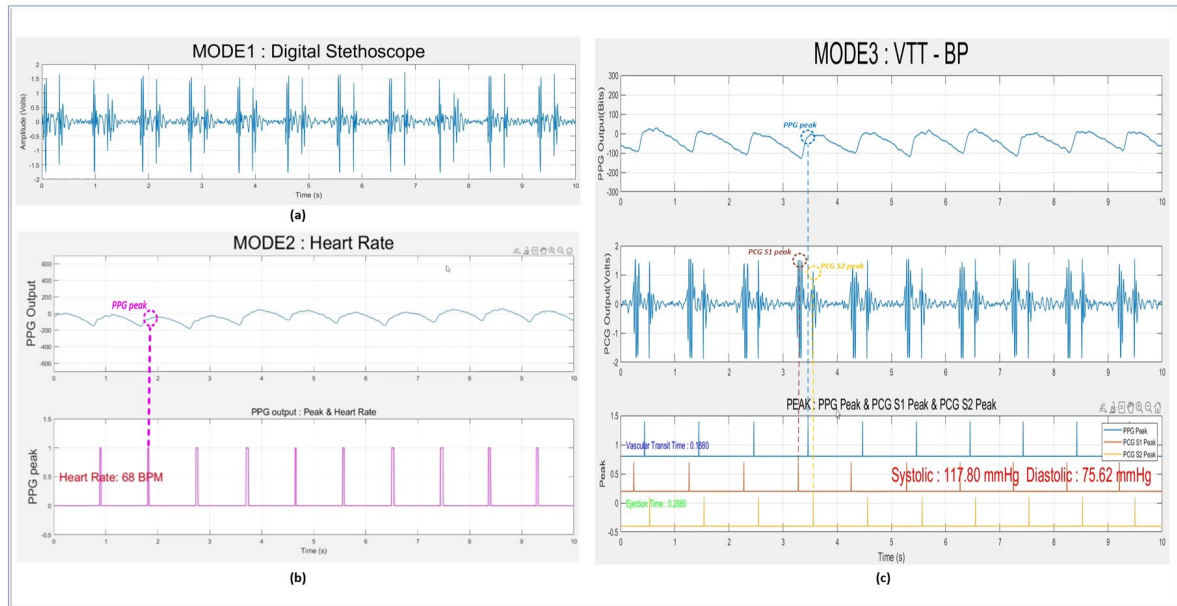
Figure 4.11. MATLAB implementation of multi-mode health monitoring system, that can be operated in (a) digital-stethoscope mode, (b) heart rate monitoring mode, and (C) VTT-based blood pressure monitoring mode

Both PPG and PCG signal can be measured through the proposed system. Thus, the proposed health monitoring system supports various monitoring mode. First, mode 1 is digital stethoscope mode. Through SAR-ADC, the PCG waveform can be checked, and the proposed system can be used as digital stethoscope. Second, mode 2 is heart rate monitoring mode. The time difference of the PPG peaks is related to heart rate. So, by extracting the peak from the PPG signal, the proposed system can be utilized for heart rate monitor. Third, mode 3 is VTT- based blood pressure monitoring mode. As described in the previous chapter, the blood pressure can be estimated from the PPG peak and the PCG peaks. Therefore, the proposed system can be utilized in wearable blood pressure monitoring system. The PCG waveform through SAR-ADC can be excluded to save the power consumption of ROIC.

All of the signal is measured on the chest. So, multi-mode health monitoring system is implemented on the chest. The real-time measurement results are transmitted from Bluetooth in the MCU to PC MATLAB program. Hence, the results of all monitoring mode are shown in PC MATLAB program, as shown in figure 4.11.

Chapter V

Summary and Conclusion

5.1 Summary

Through this master's thesis, the photoplethysmogram and phonocardiogram readout integrated circuits were designed, and blood pressure monitoring system on the chest was proposed with the designed ROIC.

Since the photodiode current from a reflected light consists of a large DC component, large DC baseline cancellation is required to prevent the output saturation of a readout circuit. For this purpose, an auxiliary DC cancellation current DAC is widely used and makes the operation of ROIC stable. However, this auxiliary current DAC has linearity problem due to the mismatch on a chip fabrication process, which interferes with getting an accurate PPG waveform. This linearity problem was solved by the DEM method. On the chest, the reflected light is attenuated because of the thick tissue, and the PPG signal has a small signal amplitude. Therefore, for the chest PPG readout, high SNR is required for ROIC. The noise performance of a conventional dual-slope LDC is limited by the noise of the core amplifier and the quantization noise. The noise of the core amplifier was removed by chopper-stabilization technique. The quantization noise was reduced by the improved noise-shaping loop which has good noise-shaping performance with a small area, and the charge sharing problem is solved, caused by the implementation of the noise-shaping loop.

Phonocardiogram AFE consists of CCIA and PGA. The PCG signal can be measured without a stethoscope through CCIA, which is a low-noise amplifier, and PGA, which can control the gain of amplifier according to signal amplitude.

For VTT-based blood pressure estimation, the time difference between two different peaks of the PCG signal, the PCG S1 peak and PCG S2 peak, and the PPG peak is required. Since two types of peaks are detected from one PCG signal, conventional analog peak detector cannot be used. Thus, dual peak detector was proposed which consists of parallel envelope detector, then PCG S1 peak and PCG S2 peak can be distinguished. With this peak detection circuits, digital processing burden and the power consumption of the MCU decreased.

The previous VTT-based blood pressure monitoring system measures the PPG signal on the finger, and should be needed a stethoscope. Hence, it interferes with our activities, and could not be implemented in wearable device and unsuitable for continuous blood pressure monitoring in daily life. The prototype was designed in a single PCB substrate integrating a photodiode and LED for PPG, a condenser microphone for PCG, ROIC, and MCU. Through this, the system with a miniaturized wearable device was implemented.

The proposed system was operated three modes: PCG based digital stethoscope mode, PPG based heart rate monitoring mode, and VTT-based blood pressure monitoring mode. For verification, the comparison of the blood pressure measurement results with a commercial blood pressure gauge was conducted.

5.2 Conclusion

This master's thesis describes the photoplethysmogram and phonocardiogram integrated circuits for the system of vascular transit time-based blood pressure estimation. The previous VTT-based blood pressure monitoring system was very uncomfortable, and could not be applied to wearable devices. Hence, through the proposed work, another solution is proposed that can be applied to wearable devices and measures physiological signal conveniently in our daily life. To measure the PPG signal on the chest, the ROIC should have a high SNR. Therefore, low-noise circuit techniques are adopted such as chopper-stabilization technique and improved noise-shaping loop. For VTT calculation and blood pressure estimation, two different peaks of PCG signal are required, then a new dual peak detector is proposed that distinguishes two different peaks in one period. Through the proposed peak detection method, the processing burden and the power consumption of MCU can be reduced. The prototype integrates sensors, ROIC, MCU, and operates using a battery. Also, it has a miniaturized size that makes it convenient to wear. By the comparison results of a commercial blood pressure gauge, it is confirmed that the proposed system has good accuracy in blood pressure estimation. The proposed system supports not only blood pressure measurement but also heart rate monitoring and can be used as a digital stethoscope. As a results, the proposed system opens opportunities for research on compact, high performance chest wearable devices which can be utilized in multi-mode healthcare system.

References

1. L. Donga, R. K. Raj and S. Mishra, "Internet of Healthcare Things (IoHT): Towards a Digital Chain of Custody," 2022 IEEE 10th International Conference on Healthcare Informatics (ICHI), 2022, pp. 524-526.

2. (2017). [Online]. Available: https://www.cdc.gov/bloodpressure/facts.htm

3. IEEE Standard for Wearable Cuffless Blood Pressure Measuring Devices, Standard 1708-2014, 2014.

4. Allen J, "Photoplethysmography and its application in clinical physiological measurement," Physiol Meas, 2007 Mar,28(3):R1-39, Epub 2007 Feb 20.

5. G. Wang, M. Atef and Y. Lian, "Towards a Continuous Non-Invasive Cuffless Blood Pressure Monitoring System Using PPG: Systems and Circuits Review," in IEEE Circuits and Systems Magazine, vol. 18, no. 3, pp. 6-26, thirdquarter 2018.

6. F. Marefat, R. Erfani and P. Mohseni, "A 1-V 8.1-μW PPG-Recording Front-End With > 92-dB DR Using Light-to-Digital Conversion With Signal-Aware DC Subtraction and Ambient Light Removal," in IEEE Solid-State Circuits Letters, vol. 3, pp. 17-20, 2020.

7. M. Alhawari, N. A. Albelooshi and M. H. Perrott, "A 0.5 V < 4μW CMOS Light-to-Digital Converter Based on a Nonuniform Quantizer for a Photoplethysmographic Heart-Rate Sensor," in IEEE Journal of Solid-State Circuits, vol. 49, no. 1, pp. 271-288, Jan. 2014.

8. C. J. Pujary, "Investigation of photodetector optimization in reducing power consumption by a noninvasive pulse oximeter sensor," M.S. thesis, Worcester Polytechnic Inst., 2004.

9. Varghees, Nivitha & K I, Ramachandran, "A novel heart sound activity detection framework for automated heart sound analysis," Biomedical Signal Processing and Control, 13, 174–188, 2014.

10. Brenton Alexander, Maxime Cannesson, Timothy J. Quill, "Chapter 12 - Blood Pressure Monitoring", Anesthesia Equipment (Second Edition), W.B. Saunders, Pages 273-282, 2013.

11. K. Yuki and H. Tsuyoshi, "Sensor technology to realize continuous blood pressure monitoring," (in Japanese), Omron Technics, vol. 50, no. 4, pp. 26-34, 2019.

12. Y. Kurylyak, K. Barbe, F. Lamonaca et al., "Photoplethysmogrambased blood pressure evaluation using Kalman filtering and neural networks," in Proc. IEEE Int. Symp. Medical Measurements and Applications, 2013, pp. 170–174.

13. Chandrasekaran V, Dantu R, Jonnada S, Thiyagaraja S, Subbu KP., "Cuffless differential blood pressure estimation using smart phones," IEEE Trans Biomed Eng, 2013 Apr.

14. S. N. Shukla et al., "Noninvasive cuffless blood pressure measurement by vascular transit time," 2015 28th International Conference on VLSI Design, 2015, pp. 535-540.

15. Q. Lin et al., "A 119dB Dynamic Range Charge Counting Light-to-Digital Converter For Wearable PPG/NIRS Monitoring Applications," in IEEE Transactions on Biomedical Circuits and Systems, vol. 14, no. 4, pp. 800-810, Aug. 2020.

16. Q. Lin et al., "A 134 DB Dynamic Range Noise Shaping Slope Light-to-Digital Converter for Wearable Chest PPG Applications," in IEEE Transactions on Biomedical Circuits and Systems, vol. 15, no. 6, pp. 1224-1235, Dec. 2021.

17. J. A. Fredenburg and M. P. Flynn, "A 90-MS/s 11-MHz-Bandwidth 62-dB SNDR Noise-Shaping SAR ADC," in IEEE Journal of Solid-State Circuits, vol. 47, no. 12, pp. 2898-2904, Dec. 2012.

18. Kamel Mars, Shoji Kawahito, "A single-ended CMOS chopper amplifier for 1/f noise reduction of n-channel MOS transistors," IEICE Electronics Express, 2012, Volume 9, Issue 2, Pages 98-103.

19. I. Galton, "Why Dynamic-Element-Matching DACs Work," in IEEE Transactions on Circuits and Systems II: Express Briefs, vol. 57, no. 2, pp. 69-74, Feb. 2010.

20. Lee, K., Chae, H.Y., Park, K., Lee, Y., Cho, S., Ko, H., Kim, J.J., "A Multi-Functional Physiological Hybrid-Sensing E-Skin Integrated Interface for Wearable IoT Applications," IEEE Transactions on Biomedical Circuits and Systems 13, 1535–1544, 2019

21. STMicroelectronics, "Multiprotocol wireless 32-bit MCU Arm®-based Cortex®-M4 with FPU, Bluetooth® 5.3 and 802.15.4 radio solution," STM32WB55cxx datasheet, 12 Aug 2022.